AGU100 ADVANCING EARTH AND SPACE SCIENCE

JGR

Journal of Geophysical Research: Oceans

RESEARCH ARTICLE

10.1029/2018JC013907

Key Points:

- An unprecedented set of in situ observations is used to determine the pathways of the water masses close to the western boundary near 34°S
- The water masses present a well-defined zonal structure characterized by primary types close to the slope and subvarieties farther offshore
- Previously undetected recirculation cells and strong meandering are observed at the intermediate and deep levels

Correspondence to:
D. Valla,
dvalla@hidro.gov.ar

Citation:
Valla, D., Piola, A. R., Meinen, C. S., & Campos, E. (2018). Strong mixing and recirculation in the northwestern Argentine Basin. *Journal of Geophysical Research: Oceans*, *123*, 4624–4648. https://doi.org/10.1029/2018JC013907

Received 13 FEB 2018
Accepted 31 MAY 2018
Accepted article online 7 JUN 2018
Published online 5 JUL 2018

©2018. American Geophysical Union. All Rights Reserved.

Strong Mixing and Recirculation in the Northwestern Argentine Basin

Daniel Valla[1], Alberto R. Piola[1], Christopher S. Meinen[2], and Edmo Campos[3]

[1]Departamento Oceanografía, Servicio de Hidrografía Naval, Departamento Ciencias de la Atmósfera y los Océanos, Facultad de Ciencias Exactas y Naturales, Universidad de Buenos Aires, and UMI/IFAECI, CONICET, Buenos Aires, Argentina, [2]Atlantic Oceanographic and Meteorological Laboratory, Miami, FL, USA, [3]Instituto Oceanográfico, Universidade de São Paulo, São Paulo, Brazil

Abstract The Atlantic component of the Meridional Overturning Circulation (AMOC) is a key contributor to the global meridional transport of volume, salt, and heat, and thus plays a central role in global climate. As part of ongoing efforts to monitor the intensity and variability of the AMOC in the South Atlantic, hydrographic sections have been regularly occupied since 2009 near the western boundary along a zonal line at 34.5°S. Here this high-quality, high-resolution data set is analyzed to establish the average hydrographic conditions of the northwestern Argentine Basin and the water mass spatial and temporal variability. The water mass analysis also reveals the pathways of the flow in this region, which are further corroborated by full-depth direct velocity measurements. The repeated hydrographic sections capture an extremely rich vertical structure, characterized by seven distinct water mass layers of northern and southern origin, each with unique property signatures. Almost all of these layers exhibit a sharp zonally banded structure, which is indicative of recirculation cells offshore from the western boundary. The circulation at intermediate levels includes a previously undetected recirculation cell confined very close to the western boundary and superimposed on the classical intermediate water pathway beneath the South Atlantic subtropical gyre. The deep level flow is characterized by the Deep Western Boundary Current (DWBC) and a northward recirculation ~500 km east from the slope.

1. Introduction

The Atlantic component of the Meridional Overturning Circulation (AMOC) consists of a northward flow of relatively warm waters in the upper ocean, deepwater formation at high latitudes in the North Atlantic and a southward flow of cold waters at depth. Together with the water volumes carried by this circulation, the AMOC redistributes massive amounts of heat through the Atlantic Ocean. At its maximum (near 24°–26°N), the northward heat transport associated with the AMOC contributes with almost 25% of the combined global atmosphere and ocean northward heat transport (Trenberth & Caron, 2001). Global circulation models consistently indicate that the AMOC may have a profound impact on the climate system variability, for example, by driving the Atlantic Multidecadal Oscillation (Zhang et al., 2014; Zhang & Wang, 2013). Changes in the AMOC are thought to have led to rapid climate change in the past: paleo-records (Peterson et al., 2000; Stott et al., 2002) as well as climate models (Ganopolski & Rahmstorf, 2001) closely relate drastic changes in the AMOC with abrupt changes in Earth's climate. Long-term climatic predictions suggest that a collapse in the overturning cell will cause an overall temperature decrease over the Northern Hemisphere, changes in African and Indian monsoon regimes, and changes in hurricane activity (Vellinga & Wood, 2002).

The AMOC is formed by a complex system of thermohaline and wind-driven currents. In this context, the energetic western boundary currents play a major role in redistributing and exchanging heat and properties. A significant portion of the cold lower limb flow of the AMOC is conveyed by the Deep Western Boundary Current (DWBC), which rapidly transports recently formed North Atlantic Deep Water (NADW) southward along the continental slope of the American continents (e.g., Bower & Hunt, 2000; Garzoli et al., 2015; Rhein et al., 2015; Watts, 1991), although ocean interior pathways are also thought to be important for the export of NADW from its source regions (e.g., Bower et al., 2009; Lozier et al., 2013). In the subtropical North Atlantic, most of the northward flowing warm upper limb of the AMOC is carried within the Gulf Stream through the Straits of Florida or in shallow western boundary currents east of the Bahamas (e.g., Frajka-Williams et al., 2016; McCarthy et al., 2015). In the subtropical South Atlantic, the warm upper AMOC limb is thought to be primarily in the eastern basin (Garzoli et al., 2015). However, the western

boundary currents in the upper and intermediate levels may also have an important role in driving the South Atlantic AMOC (i.e., "SAMOC") variability locally, for example, by modifying the density field of the upper water column (Dong et al., 2014). Additionally, the western boundary current in the upper layer transports heat southward, that is, opposite to the SAMOC (Dong et al., 2009). To achieve a comprehensive characterization of the AMOC, several observing systems have been deployed in the North Atlantic to continuously measure its strength and variability, such as the Meridional Overturning Variability Experiment (MOVE) and the 26°N MOC array, among others (e.g., Perez et al., 2015; Send et al., 2011; Srokosz & Bryden, 2015). Theoretical and modeling studies have suggested that significant AMOC variability and water mass transformation may be originated in the South Atlantic (Garzoli & Matano, 2011). In order to continuously monitor the SAMOC, a trans-basin mooring line along 34.5°S known as the South Atlantic MOC Basin-wide Array ("SAMBA") has been under development since March 2009. The western portion of the SAMBA mooring array (hereafter referred to as the SAMBA-W mooring line) consists of four pressure-equipped inverted echo sounders (PIESs), two current-and-pressure equipped inverted echo sounders (CPIESs), and at times a bottom pressure recorder and a bottom-mounted acoustic Doppler current profiler (Meinen et al., 2012, 2013, 2017); the eastern portion comprises eight CPIES moorings combined with four tall moorings distributed along the continental slope near South Africa (Ansorge et al., 2014).

The SAMBA-W mooring line is located in the northwest Argentine Basin, a convergence region for multiple water masses of northern and southern origin (Figure 1a). The main component of the upper circulation in this region is the Brazil Current (BC), representing the western boundary current of the South Atlantic subtropical gyre. The flow of the BC begins in the subtropics, fed by the westward flowing South Equatorial Current (SEC). As the SEC waters reach the coast of South America near 15°S, a portion feeds the North Brazil Current, and the remainder flows poleward along the continental slope as the BC (Figure 1a). In the subtropical South Atlantic, the upper portion of the intermediate circulation (typically 500–1,200 m) is coupled with the surface gyre (e.g., Gordon et al., 1992; Piola & Georgi, 1982; Reid, 1989; Rintoul, 1991). The northern branch of the intermediate circulation flows westward and reaches the South American continental margin in the southern portion of the Santos Basin near 27°S (Figure 1a). This area is referred to as the "Santos Bifurcation" because here the intermediate flow splits into two branches, one turning equatorward and feeding the North Brazil Undercurrent and the other turning poleward beneath the BC as an Intermediate Western Boundary Current (IWBC; Boebel et al., 1999; Legeais et al., 2013). Adjusted steric height charts show a similar circulation pattern for the lower intermediate circulation (typically 1,200–2,000 m; Reid, 1989). The deep circulation (typically 2,000–3,500 m) is characterized by a well-defined DWBC, which mainly transports recently ventilated NADW southward (Reid et al., 1977). Direct current measurements indicate that the DWBC breaks into eddies at 8°S (Dengler et al., 2004). According to recent estimates from ship surveys and from moored observations during the period 2013–2014, the DWBC transport is still carried primarily by deep eddies (Hummels et al., 2015). The presence of a continually flowing DWBC along the western boundary has been reported farther south between 20° and 28°S (Müller et al., 1998; Zangenberg & Siedler, 1998). Hydrographic and chlorofluorocarbon data, and several numerical models, also suggest that a small fraction (22%) of the recently ventilated NADW spreads toward the east between ~17° and 25°S (Garzoli et al., 2015). The abyssal flow in the Argentine Basin (typically deeper than 3,500 m) has been historically inferred from cross-shore sections and horizontal charts of isopycnal surfaces and other properties near the sea bottom (Georgi, 1981a; Reid et al., 1977). These data suggest that cold and dense waters mainly formed in the Weddell Sea enter the basin around the Islas Orcadas Rise and through two deep passages (~5,000 m) located east of the Malvinas Escarpment and circulate cyclonically along the western edge of the basin (Figure 1a). At ~38°S, a portion recirculates into the interior while another branch continues northward and is exported to the Brazil Basin through the Vema Channel and the Hunter Channel (Georgi, 1981a; Speer & Zenk, 1993). Based on historical data, Coles et al. (1996) found evidence of a northeastward abyssal flow in the vicinity of the SAMBA-W line.

The SAMBA-W line is located just north of the confluence of the BC and the Malvinas Current (MC), known as the Brazil-Malvinas Confluence (BMC), one of the most energetic regions of the world ocean (Garzoli, 1993; Gordon & Greengrove, 1986b; Lumpkin & Garzoli, 2011; Figures 1b and 1c). Typical eddy kinetic energy (EKE) values of ~2,000 cm^2/s^2 are observed in the vicinity of the BMC, whereas EKE values do not exceed ~600 cm^2/s^2 nearby SAMBA-W (Figure 1b). Thus, observations at this latitude are key to determine the western boundary circulation as close as possible to the southern limits of the subtropical gyre while avoiding the strong variability associated with the BMC. The goal of this paper is to characterize the time-averaged zonal

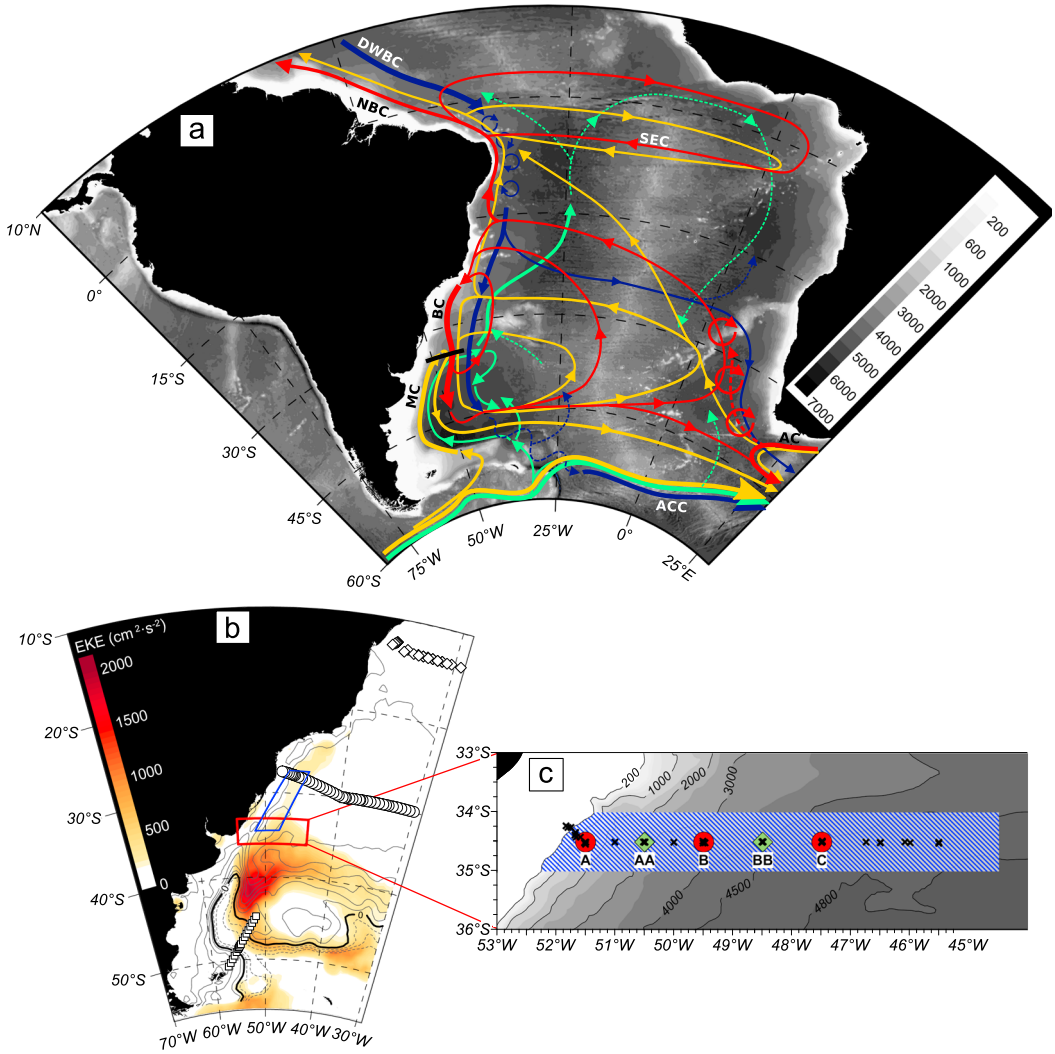

Figure 1. (a) Schematic of the main components of the South Atlantic large-scale circulation. The color-coded paths represent the flow at different vertical levels: upper (TW/SACW, red), intermediate (AAIW/UCDW, yellow), deep (NADW, blue), and abyssal (LCDW/AABW, light green). The names of the main currents are indicated: Agulhas Current (AC), Antarctic Circumpolar Current (ACC), Brazil Current (BC), Deep Western Boundary Current (DWBC), Malvinas Current (MC), North Brazil Current (NBC), and South Equatorial Current (SEC). The base map is adapted from Lumpkin and Speer (2007) and Speich et al. (2007); see also references in text. The thick black line represents the SAMBA-W mooring line. (b) Locations of historical CTD stations collected during CLIVAR/WOCE A10 (circles), CITHER-2 LEG 1 (WOCE A17, squares), and CITHER-2 LEG 2 (diamonds) sections. The blue box in the western boundary indicates the region where Argo profiles were selected to prepare Figures 5 and 6. The red box indicates the domain shown in (c). The background colors represent the eddy kinetic energy (EKE, cm^2/s^2), and the black contours represent the mean absolute dynamic topography (the contour spacing is 10 cm, and the dashed contours represent negative values) between 1993 and 2016 derived from satellite altimetry. (c) Area of work of the SAMBA-W line within the SAMOC initiative. The red circles (green diamonds) are the location of the PIES (CPIES), and the crosses are the CTD stations occupied along SAMBA-W. The blue hatched box is the area where Argo profiles were selected to prepare Figures 3 and 4. The background in (a) and (b) represents the bottom topography in m from GEBCO (IOC et al., 2003).

structure of the water masses at the SAMBA-W line and to determine the average pathways of these water masses in the vicinity of 34.5°S. To this end, we report a new set of hydrographic data with unprecedented time-space resolution, collected along the SAMBA-W line. We also analyze some aspects of the temporal variability of the water properties, although we do not pursue a full analysis of the mesoscale processes associated with these variations because our current data set (essentially, a half-dozen snapshot hydrographic sections spread over four years) cannot resolve high-frequency (mesoscale) activity. The data and methods are presented in sections 2 and 3, respectively. In section 4, the time-averaged properties of

Table 1
Hydrographic and LADCP Data Included in This Study

Cruise	Date	Data source	Data type
CITHER-2 (LEG 1, WOCE A17)	4 January to 23 February 1994	(Mémery et al., 1995)	CTD
CITHER-2 (LEG 2, WOCE A17)	17 February to 21 March 1994	(Mémery et al., 1995)	CTD
CLIVAR BEAGLE 2003 (WOCE A10)	6 November to 5 December 2003	(Uchida et al., 2005)	CTD
CLIVAR A10 (WOCE A10)	26 September to 31 October 2011	(Wanninkhof et al., 2013)	CTD
SAM02	20–24 August 2009	This study	CTD
SAM03	5–16 July 2010	This study	CTD
SAM04	20–29 December 2010	This study	CTD
SAM05	2–12 July 2011	This study	CTD/LADCP
SAM07	2–11 July 2012	This study	CTD/LADCP
SAM08	1–16 December 2012	This study	CTD

the water masses as well as their time variations are presented and discussed in the context of the general circulation. On the basis of these results, pathways for each layer are proposed. A summary and concluding remarks are presented in section 5.

2. Data

As part of the SAMOC initiative (www.aoml.noaa.gov/phod/SAMOC_international), six Conductivity-Temperature-Depth (CTD) sections were occupied along the SAMBA-W line between July 2009 and December 2012 using two different research vessels (Table 1). Five occupations were completed using the R/V *Puerto Deseado*, and one (SAM08) using the R/V *Alpha-Crucis*. Full-depth CTD profiles are available for all occupations (the station locations are shown in Figure 1c). High-quality, quasi-continuous profiles of temperature (T), salinity (S), and dissolved oxygen concentration (O_2) were collected and subsampled at 1 dbar intervals at every station together with up to 24 bottle samples for calibration. CTD measurements were collected using SBE 3plus and SBE 3-02/F temperature, SBE 4C and SBE 4-02/O conductivity, and SBE 43 oxygen sensors attached to a SBE 9/11+ CTD. The conductivity of each bottle sample was determined using Guildline AUTOSAL salinometers from which bottle salinity was derived with an uncertainty of ±0.003. CTD salinity data were then calibrated against bottle samples, and an uncertainty of ±0.003 was estimated for the final calibrated CTD salinity measurements. Likewise, the dissolved oxygen concentration of each bottle sample was determined with the Winkler titration method (Langdon, 2010), and CTD oxygen data were calibrated against the bottle samples. An uncertainty of ±5 μmol/kg was estimated for the final CTD oxygen measurements. Because there were no oxygen water samples collected during SAM02, oxygen data from this cruise were excluded from the analysis. In addition, a Teledyne RD Instruments 300 kHz Workhorse Monitor lowered-Acoustic Doppler Current Profiler (LADCP) was deployed together with the rosette multisampler during the SAM05 and SAM07 cruises (Table 1).

Delayed mode Argo pressure (P), T and S profiles collected from 2003 to December 2016 within the region bounded by 34°S, 35°S, 44.5°W and the shelf break (Figure 1c) were combined with the above indicated CTD data to prepare mean salinity and potential temperature sections presented in section 4.1. All available Argo profiles were used instead of limiting to the 2009–2012 time window when the CTD sections along the SAMBA-W line were occupied in order to increase the number of available Argo profiles. Additional Argo data were used to determine the thermohaline properties close to the western boundary north of the SAMBA-W line (blue box in Figure 1b). The Argo data were obtained from the U.S. NODC World Ocean Database 2013 available at http://www.nodc.noaa.gov/OC5/WOD/pr_wod.html (Boyer et al., 2013). All profiles with a WOD Quality Flag higher than 2 were excluded from the analysis. The remaining profiles were visually inspected and compared with the CTD data set collected at SAMBA-W to detect any noticeable sensor drifts or offsets. Additional historical hydrographic data were used to investigate the properties of the water masses at the western boundary of the South Atlantic north and south of the SAMBA-W line as presented in section 4.1 (Table 2). The CTD data across the Malvinas Escarpment between ~51 and ~45°S correspond to the WOCE line A17 and were obtained from the CITHER-2 project archive (Mémery et al., 1995), as well as the data along the section near 13°S (Mémery et al., 1995). The CTD data at the western edge of the Santos Basin near 30°S correspond to two CLIVAR A10 occupations in 2003 and 2011 (Uchida et al., 2005; Wanninkhof et al., 2013). The

Table 2
Neutral Density (γ, kg/m^3) Range Assign for Each Water Mass Layer[a]

Water mass	γ range	θ (°C)	S	O_2 (μmol/kg)
TW	<26.35	19.75	36.09	225
SACW	26.35–27.10	12.10	35.10	211
AAIW	27.10–27.60	4.05	34.245	237
UCDW	27.60–27.90	2.90	34.58	188
NADW	27.90–28.10	2.95	34.91	241
LCDW	28.10–28.27	0.72	34.72	215
AABW	>28.27	−0.10	34.67	226

Note. The zonally averaged potential temperature (θ), salinity (S), and dissolved oxygen (O_2) values at the center of each range computed from all cruises occupied at the SAMBA-W line are given as a reference.
[a]TW: Tropical Water; SACW: South Atlantic Central Water; AAIW: Antarctic Intermediate Water; UCDW: Upper Circumpolar Deep Water; NADW: North Atlantic Deep Water; LCDW: Lower Circumpolar Deep Water; AABW: Antarctic Bottom Water.

stations locations are shown in Figure 1b. Also shown are the EKE and the mean absolute dynamic topography (ADT) for the period 1993–2016 (Figure 1b). The mean EKE was computed from surface geostrophic velocities with a horizontal resolution of 1/4° produced and distributed by E.U. Copernicus Marine Service Information (product identifier SEALEVEL_GLO_PHY_L4_-REP_OBSERVATIONS_008_047). The mean ADT (i.e., sea surface height above geoid) was downloaded from AVISO (http://www.aviso.altimetry.fr).

3. Methods

The mean vertical sections presented in section 4.1 are prepared by linearly interpolating the CTD and Argo profiles onto a regular density grid using neutral density (γ; Jackett & McDougall, 1997) as the vertical coordinate, which is computed using the "GAMMA-N" γ package version 3.1 for Matlab. The data are interpolated along 34.5°S at γ intervals of 0.02 kg/m^3 for 25.00 kg/m^3 $< \gamma <$ 27.60 kg/m^3 and 0.005 kg/m^3 for 27.60 kg/m^3 $< \gamma <$ 28.29 kg/m^3 and at distance intervals of 49 km. The distance origin is set at (51.5°W, 34.5°S), where the section changes orientation from zonal to southeast-northwest (site A, Figure 1c). Before gridding, Argo profiles within the selected region were projected onto 34.5°S following the mean orientation of the shelf-break (~43.5°T). Diluted waters from the Río de la Plata occasionally occupy the upper ~50 m of the southern Brazil outer shelf and shelf break, extending as far north as 28°S during fall-winter and spreading farther offshore in spring-summer (Piola et al., 2000). The variability introduced by these low salinity waters is beyond the scope of this study. Thus, data exhibiting these waters are excluded from the analysis by removing the upper 50 dbar of all CTD and Argo profiles with $S < 35$.

The neutral density boundaries used to delimit each water mass layer are determined based on water mass properties criteria similar to those adopted by Preu et al. (2013), except that only neutral density criteria are applied in this paper. The boundary between the Tropical Water (TW) and South Atlantic Central Water (SACW) was defined as the neutral density at the zonally averaged 16 °C isotherm. The neutral density ranges assigned to each water mass layer are detailed in Table 2. Constant neutral density contours are plotted in every θ-S diagram for reference. The selected γ contours are computed by fitting a quadratic function (i.e., θ as a function of S) to the data used in each diagram.

To study the hydrographic conditions in the intermediate layers near the western boundary between the SAMBA-W line and the Santos Bifurcation (~27°S), 325 Argo profiles collected within 250 km of the 200 m isobath in the cross-shore direction are inspected (blue box in Figure 1b). The profiles are sorted in three latitude bands, namely, 34.5–31.5°S, 31.5–29°S, and 29–27.5°S. The mean θ-S distribution for each band is computed by averaging the observed salinities within 0.1 °C potential temperature bins. The salinity standard deviation for each θ bin is also computed.

The temporal variability of the water mass properties is presented in section 4.2. Changes are investigated along neutral density surfaces in order to minimize the dynamic heaving effect associated with mesoscale and higher frequency features, such as the passage of eddies or internal waves. The standard deviation sections of θ, S, and O_2 are computed relative to the section mean by first gridding each separate hydrographic section as described above using only CTD data and then computing the standard deviation for each grid element relative to its mean value. The spatiotemporal structure of the water masses is further analyzed at four longitudes along the SAMBA-W line, which correspond to the locations of the PIES moorings (red circles in Figure 1c). For calibration purposes a CTD profile was collected at each of the PIES locations in all cruises, thus providing the best temporal coverage at these sites. For each of these four locations, all available P, θ, S, and O_2 profiles are linearly interpolated onto the regular γ grid defined above and averaged and standard deviation profiles are then computed.

The LADCP data are processed for horizontal velocity with the LDEO_IX implementation of the velocity inverse method (Visbeck, 2002) version 12. Due to the lack of shipboard ADCP measurements, only the ship drift measured with the GPS and the bottom tracking data (available for all profiles) were used to constrain

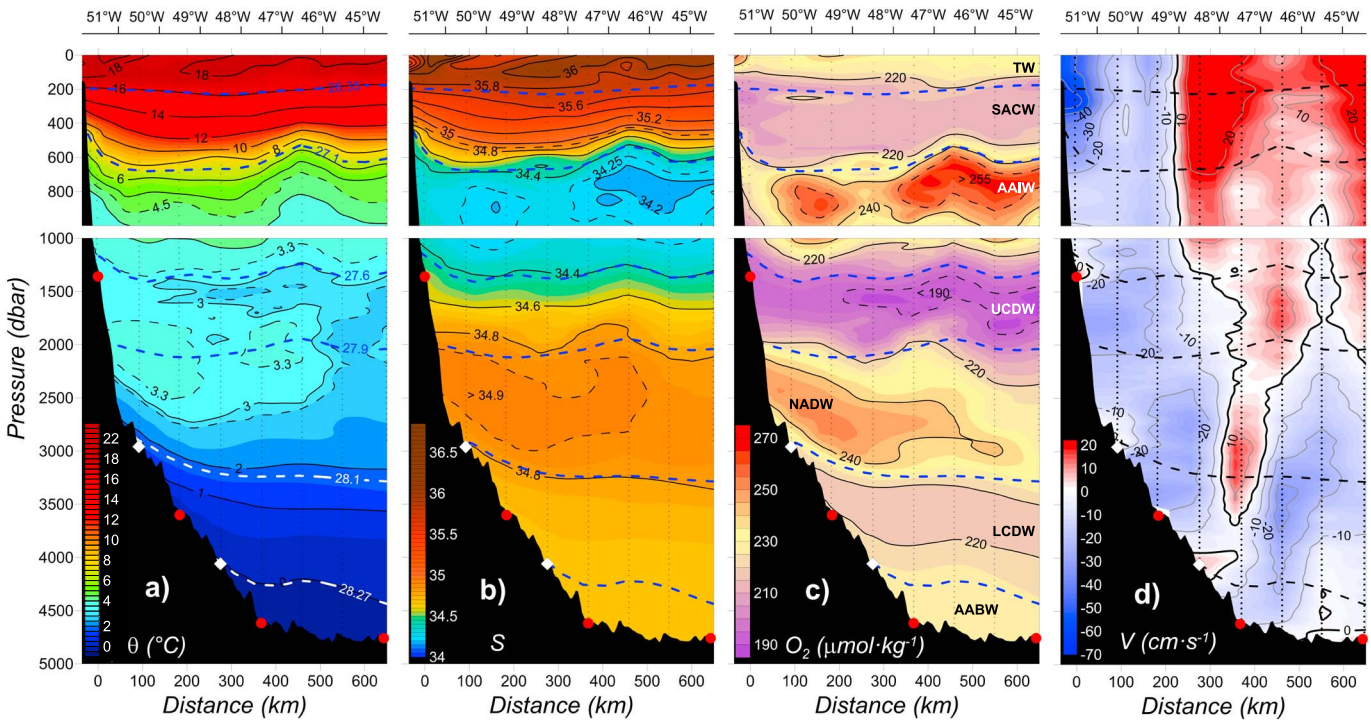

Figure 2. Synoptic sections of (a) potential temperature (θ), (b) salinity (S), (c) dissolved oxygen concentration (O_2), and (d) alongshore velocity (V) at the SAMBA-W line collected during SAM-07 cruise in July 2012. The red circles (white diamonds) in all panels indicate the PIES (CPIES) locations, and the vertical dotted lines indicate the location of the CTD/LADCP stations. The blue and white dashed lines indicate the γ surfaces used to delimit the water masses. Note that the section changes orientation west of the x axis origin (Figure 1c). The water masses are indicated in (c).

the barotropic velocities. For each profile, the horizontal velocity was projected onto a reference frame rotated 43.5°T to match the shelf break orientation. A section of the alongshore component of the velocity was created for each occupation by gridding the data in the same fashion as done for the θ, S, and O_2 data. The time-mean alongshore section was then obtained by averaging the two realizations. Higher quality profiles were typically collected west of 47°W, where the region is characterized by stronger acoustic backscatter. This is reflected by the higher instrument range observed below ~1,000 m (80–110 m) in contrast with the lower ranges observed farther offshore (60–90 m). Given these range values for a single down-looking LADCP, we have estimated the accuracy of the final LADCP data to 5 cm/s (Thurnherr, 2010). Therefore, we have neglected all velocity values below this threshold.

4. Results and Discussion

4.1. Hydrographic Structure and General Circulation in the Vicinity of the SAMBA-W Line

As a consequence of the convergence of multiple water masses formed in different regions of the world ocean, the northwestern Argentine Basin is characterized by a highly complex hydrographic structure, which can be seen in the full-depth, high-resolution sections of θ, S, and O_2 collected during the SAM07 cruise in July 2012 presented in Figure 2. These quasi-synoptic sections also reveal the presence of relatively intense mesoscale features passing through the SAMBA-W line, such as the cyclonic eddy centered at 46.5°W, which generates a significant doming of isopycnals. To complement the synoptic view of the hydrographic conditions along the SAMBA-W line, time-averaged sections including all CTD occupations and historical Argo profiles as detailed in section 2 are also presented in Figure 3. An average section of the alongshore component of the horizontal velocity derived from the LADCP measurements is also displayed to corroborate our findings regarding the main pathways of the water masses (Figure 3d). The comparison between the snapshot and the time-averaged property sections reveals a structure that sustains over time (at least over the period of a few years when the observations were collected) despite the contrasting properties between adjacent layers. Indeed, the zonally averaged time-mean θ-S and θ-O_2 diagrams (Figure 4) exhibit several inflection points, each representing distinct water masses formed at remote locations around the globe. From top to

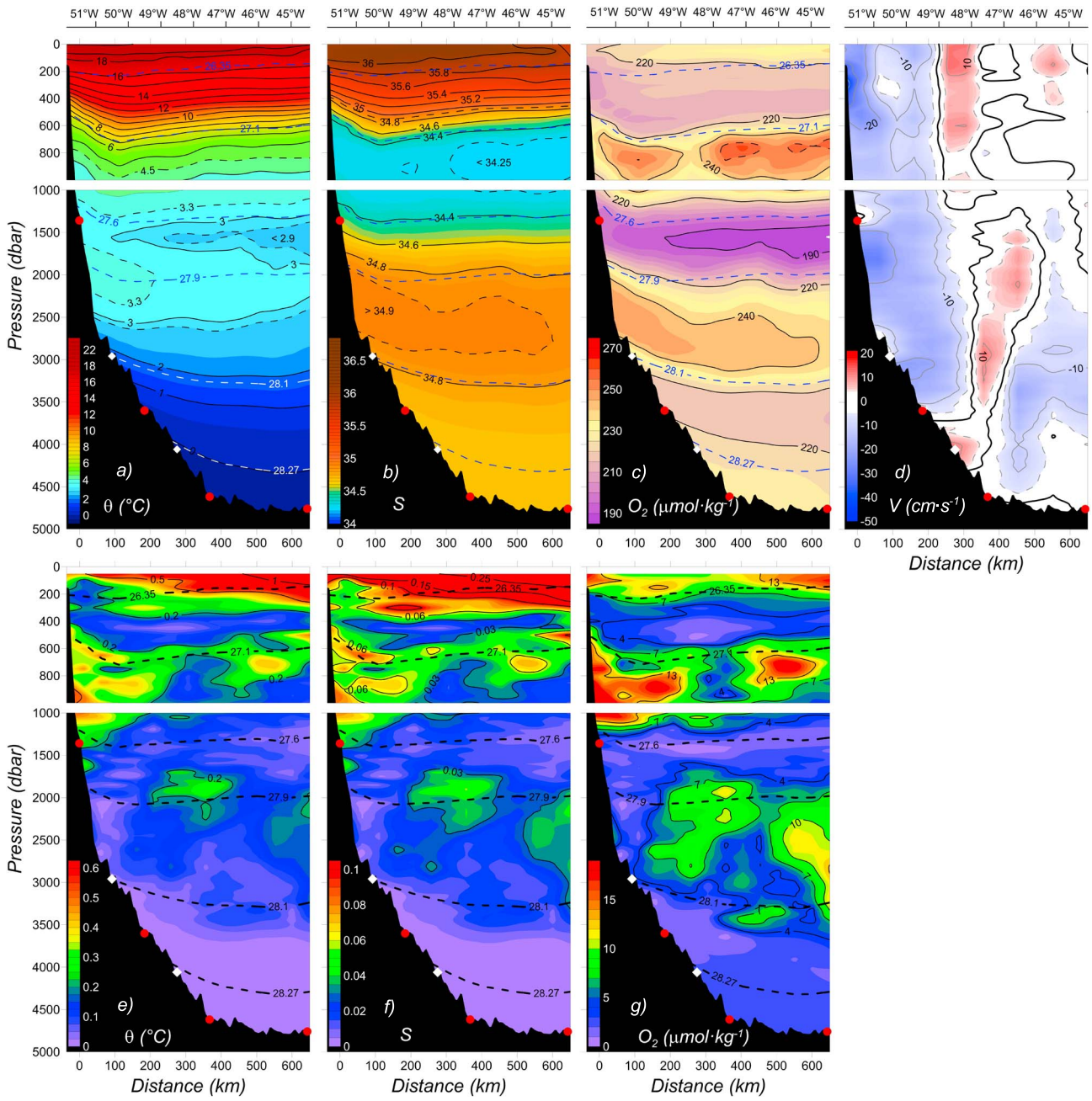

Figure 3. (a–c) Average sections of potential temperature (θ), salinity (S), and dissolved oxygen concentration (O_2) at the SAMBA-W line using all CTD profiles collected within the SAMOC initiative and all available Argo profiles in the region (see Figure 1 for CTD and Argo profiles locations). (d) Average section of the alongshore velocity (V) derived from LADCP measurements. (e–f) Standard deviation sections of θ, S, and O_2 at the SAMBA-W line using only CTD profiles collected within the SAMOC initiative. The red circles (white diamonds) in all panels indicate the PIES (CPIES) locations. The dashed lines indicate the averaged γ surfaces used to delimit the water masses. Note that the section changes orientation west of the x axis origin (Figure 1c).

bottom, the water masses are TW, SACW, Antarctic Intermediate Water (AAIW), Upper Circumpolar Deep Water (UCDW), NADW, Lower Circumpolar Deep Water (LCDW), and Antarctic Bottom Water (AABW). In what follows, the vertical and zonal structures of θ, S and O_2 of each water mass layer at the SAMBA-W line are analyzed focusing on four selected longitudes, namely, at 51.5°W, 49.5°W, 47.5°W, and 44.5°W. A comparison with historical data at other latitudes is made to infer the flow and recirculation patterns in the vicinity of the SAMBA-W line, and the results are discussed in the context of the South Atlantic western boundary circulation.

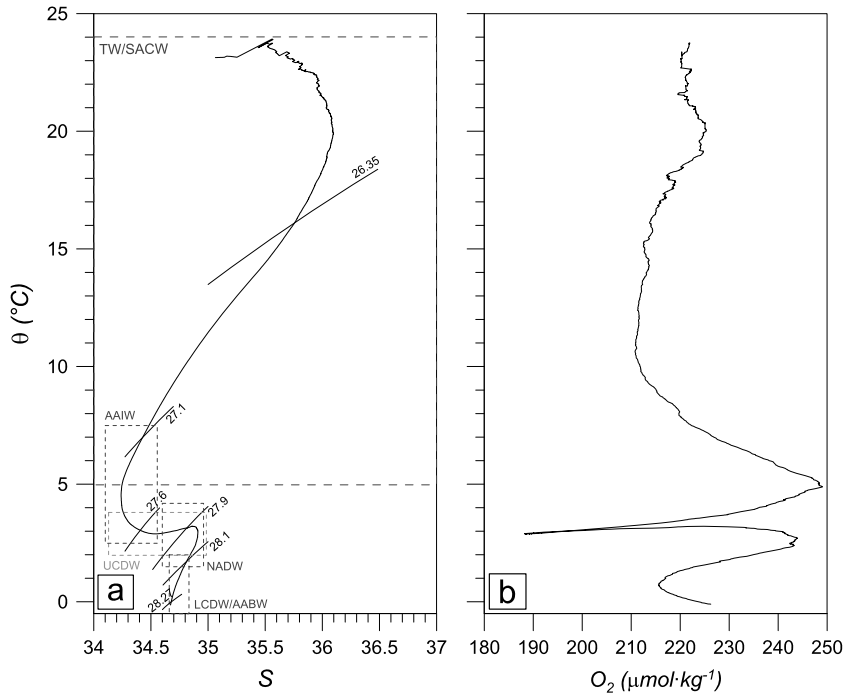

Figure 4. Zonally averaged, time-mean (a) θ-S and (b) θ-O_2 distribution along the SAMBA-W line using all CTD profiles collected within the SAMOC initiative and all available Argo profiles in the region (see Figure 1 for location). The dashed boxes in (a) indicate the domains of the water masses discussed in Figures 5–9. The solid lines are the γ surfaces used to delimit the water masses (see text for details on the determination of these).

4.1.1. Tropical Water

The upper ~200 m of the water column at the SAMBA-W line are occupied by the warm and relatively salty TW, a diluted variety of the Salinity Maximum Water (SMW) that originates in the subtropics due to excess evaporation over precipitation (Mémery et al., 2000). Due to its relative high density, the SMW is subducted below the surface as it flows south from its formation region, while its salinity decreases below 37.00 through mixing with the fresher surrounding waters. By the time the SMW reaches 34.5°S and has become TW, the core of the layer is characterized by a subsurface salinity maximum in the upper-right corner of the average θ-S diagram at θ ~ 20.0 °C, S ~ 36.10 (Figure 4a and Table 2). The averaged θ-S and O_2-S diagrams at the four selected longitudes along the SAMBA-W line are presented in Figure 5. The saltiest, least modified variety of TW is found at the westernmost location, 51.5°W, within the core of the BC (θ ~ 21 °C, S ~ 36.50). The TW becomes monotonically fresher and colder in the offshore direction (Figure 5a). For example, the salinity maximum at 44.5°W is found at θ ~ 18.7 °C and S ~ 35.98. Subsurface dissolved oxygen maxima are also observed offshore of the BC, centered at θ = 19.5 °C at 49.5°W, θ = 19.0 °C at 47.5°W, and θ = 17.0 °C at 44.5°W (Figure 5b), whereas no noticeable maximum is observed at 51.5°W.

The diluted TW observed east of 49.5°W is consistent with previous analyses of the western boundary circulation south of 34.5°S. After colliding with the MC, the BC splits into two branches, one flowing southward as an overshoot, and the other turning equatorward offshore of the BC (Stramma & Peterson, 1990; Figure 1a). After crossing the SAMBA-W line, the TW flowing southward within the BC becomes colder and fresher through mixing with subantarctic waters in the Brazil-Malvinas front. It then recirculates northward offshore of the main southward flow. Hereafter we refer to this northward countercurrent as the "BC offshore recirculation." The relatively high mean EKE observed east of ~50°W at SAMBA-W (~300–600 cm^2/s^2; Figure 1b) compared to the weak mean kinetic energy in that region (<50 cm^2/s^2, not shown) suggests that the BC offshore recirculation may be dominated by mesoscale features, such as eddies and meanders. By contrast, the mean flow is significantly more energetic closer to the western boundary, west of ~51°W, where the mean kinetic energy range is 300–400 cm^2/s^2 and the EKE is ~100 cm^2/s^2. Because the recirculated TW found within the BC offshore recirculation contains elements of subantarctic waters, there is a noticeable thermohaline contrast

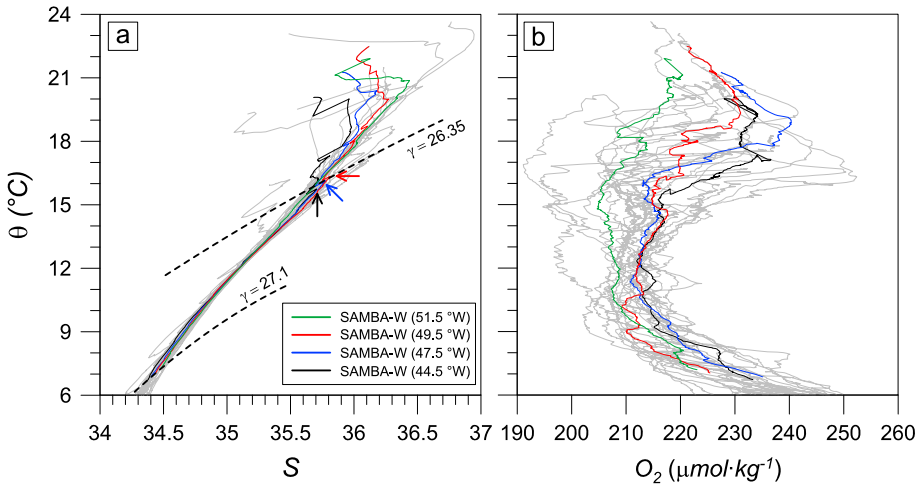

Figure 5. (a) θ-S and (b) θ-O_2 distribution for the TW/SACW layer along the SAMBA-W line. The colored curves in both panels are time averages at selected longitudes, and the grey curves are all individual CTD profiles collected within the SAMOC initiative only at these four longitudes. Averaged and individual profiles are limited to these water mass layers. The arrows indicate the inflection points in the θ-S plot at each longitude. The heavy dashed lines are the γ surfaces used to delimit the water masses.

with the more pristine TW found within the BC. The highest θ-S contrast between the TW variety found at 51.5°W and the TW variety found at 49.5°W is observed during austral summer because the waters within the BC are warmer and saltier. For example, during the SAM08 cruise (December 2012), the TW core at 51.5°W was found at $\theta \sim 23$ °C, $S \sim 36.95$, which was 2.5 °C warmer and 0.68 saltier than the TW core at 49.5°W (not shown). The oxygen maxima associated with the modified waters observed offshore are also consistent with mixing with oxygen-rich subantarctic waters. Furthermore, the inspection of individual profiles shows that the O_2 maxima are largely located at the top of the main thermocline, also suggesting an increase of dissolved oxygen concentration due to photosynthetic activity, which is known to be enhanced in the Brazil-Malvinas frontal zone (Brandini et al., 2000).

4.1.2. South Atlantic Central Water

The average SACW at the SAMBA-W line is characterized by a nearly straight line between 5 °C, 34.25 and 16 °C, 35.75 in the θ-S diagram as well as by relatively low O_2 concentrations ($O_2 < 220$ μmol/kg) in comparison with the vertically adjacent water masses (Figures 4a and 4b and Table 2). Similarly, the SACW found in the core of the BC is also represented by a straight line and is poorly oxygenated (green line in Figures 5a and 5b). Farther offshore, however, the average θ-S curves show distinct inflections at 16.3 °C–35.81 at 49.5°W, 16.1 °C–35.76 at 47.5°W, and 15.74 °C–35.70 at 44.5°W (Figure 5a). Rather than being an averaging artifact, these inflections are a result of the presence of somewhat colder and saltier waters within the upper SACW. These inflections are present during the majority of the occupations. Associated with these modified varieties, the SACW found offshore of the BC (i.e., east of 49.5°W) also shows higher O_2 concentrations. Indeed, at 51.5°W, the waters within this layer are on average ~10 μmol/kg less oxygenated than farther offshore (Figure 5b).

The SACW is mainly formed south of the SAMBA-W line, within the BMC and further east along the Subtropical Front during austral winter (Provost et al., 1999). After being subducted into the thermocline the SACW recirculates around the subtropical gyre, showing uniform properties across the basin. At the SAMBA-W line, the lower portion is characterized by a relatively low O_2 concentration (Figure 4b). The saw-toothed intrusions observed in the averaged θ-S diagram in the upper portion of the SACW of the region located offshore of the BC are typical of Subtropical Mode Water (STMW) formed through winter convection and subsequently capped by a fresher layer (Gordon, 1981). Based on historical hydrographic data, Provost et al. (1999) found that the BMC is a major region of mode water formation in the western South Atlantic and identified three main types of STMW. The salinity maxima associated with the inflections observed within SACW in the SAMBA-W line approximately fall within their STMW Type II. This water mass is characterized by $\theta = 15.0 \pm 1.0$ °C, $S = 35.60 \pm 0.15$; originates during the formation of deep winter mixed layers; and represents

the largest STMW volume. Our observations also fall into the STMW Type I as more recently defined by Sato and Polito (2014) (θ = 15.0 ± 0.9 °C, S = 35.60 ± 0.20), which is also thought to originate in the vicinity of the BMC. The influence of STMW in the BC offshore recirculation is further supported by the relatively higher dissolved oxygen concentration at the STMW temperature range ($\theta > 11.0$ °C; Figure 5b). The θ-S inflections are not observed within the BC at the SAMBA-W line because at this location the waters in this density layer are purely of northern origin. Hence, the transition between the SACW observed within the BC and the admixtures of SACW and STMW found farther offshore also suggest a northward counter flow across the SAMBA-W line east of 49.5°W. The average velocity section displays a mean southwestward flow west of ~49°W throughout the water column (Figure 3d). West of 51°W, the higher velocities are associated with the BC ($>$ 20 cm/s) and confined to the upper 600 m. The BC offshore recirculation is clearly depicted in the velocity section collected in July 2012, with alongshore velocities exceeding 20 cm/s east of 49°W (Figure 2d). The average velocity section has hints of this northeastward flow between 48 and 49°W and 46.5 and 45°W (Figure 3d).

The presence of a semipermanent recirculation cell in the upper ~500 m of the water column may have an important role in the volume transport associated with the AMOC at 34.5°S. Dong et al. (2014) have shown that changes in the net geostrophic transport across a transbasin section at this latitude, at seasonal time scales, are partially controlled by changes in the western boundary density field. The authors suggested that these density changes are associated with the relative strength of the MC and the BC, which generate positive density anomalies in the western boundary due to an intensification of the MC and a weakening of the BC during austral winter, and the opposite during summer. Although the MC does not extend as far north as 34.5°S, a northward excursion during winter could effectively enhance the mixing of subtropical and subantarctic waters across the Brazil-Malvinas Front within the TW and SACW layers, resulting in colder and fresher waters being advected northward by the BC offshore recirculation, which would generate positive density anomalies near 34.5°S.

4.1.3. Antarctic Intermediate Water

The relatively fresh and highly oxygenated AAIW is injected into the South Atlantic through two routes, one with the MC which is relatively colder and fresher (Piola & Gordon, 1989), and another from the Indian Ocean as part of the Agulhas/Benguela current system, which conveys a relatively warmer, saltier, and less oxygenated variety (Lutjeharms, 1996; Piola & Georgi, 1982; Talley, 1996; Figure 1a). Some of the AAIW sources may also enter the South Atlantic by subduction just south of the Subantarctic Front throughout the basin (Schmid, 2000). Near the western boundary, the AAIW flows poleward south of ~27°S. This is confirmed by the offshore deepening of isopycnals over the shelf break along the SAMBA-W line, observed in both the synoptic and the averaged sections ($<$130 km; Figures 2 and 3), which sustains a southward geostrophic flow relative to the BC. The averaged salinity and the dissolved oxygen sections show an AAIW that is somewhat saltier and less oxygenated beneath the BC than farther offshore (Figures 3a–3c). Recall that the averaged sections include data from ~300 Argo profiles collected in the vicinity of the SAMBA-W line during a 12-year span, hence suggesting that this asymmetry is a semipermanent feature of the AAIW layer in this region. To further investigate this structure, the averaged θ-S and θ-O_2 properties in the AAIW γ range at the four selected longitudes along the SAMBA-W line are presented in Figure 6. The core of AAIW (γ = 27.34 kg/m^3) at the two western locations, 51.5°W and 49.5°W, is saltier than 34.25 and exhibits oxygen concentrations lower than 250 μmol/kg, whereas it is ~0.25 °C colder, 0.02 fresher, and 10–15 μmol/kg higher in O_2 further east at 47.5°W and 44.5°W (colored curves in Figures 6a and 6b). Furthermore, the analysis of AAIW properties at the western boundary north and south of the SAMBA-W line shows that the waters found beneath the BC at 34.5°S are closer to those observed farther north near the Santos Bifurcation ($S > 34.28$, $O_2 < 235$ μmol/kg; gray circles in Figures 6a and 6b), whereas the waters observed offshore at 34.5°S resemble those found near the Malvinas Escarpment ($S < 34.2$, $O_2 > 260$ μmol/kg; black crosses in Figures 6a and 6b).

To extend these results, we study the AAIW hydrographic structure at the western boundary between the SAMBA-W line and the Santos Bifurcation using Argo data as explained in section 3. Note that Argo profiles are limited to 250 km from the 200 m isobath so as to include only the saltier and less oxygenated variety of AAIW found onshore at the SAMBA-W line (Figures 3b and 3c). The results are presented in the inset in Figure 6a. An overall north-to-south salinity decrease is observed in the averaged Argo profiles. At 4.5 °C, the salinity is on average 34.255 between 34.5°S and 31.5°S, 34.290 between 31.5°S and 29°S, and 34.320 at 29°S–27.5°S. Despite the difference in the number of averaged Argo profiles at the three latitude bands

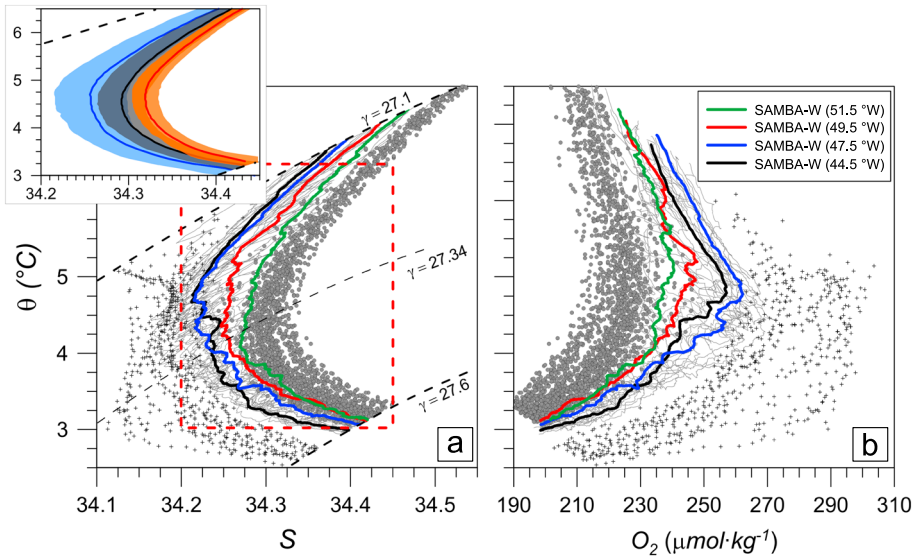

Figure 6. Same as Figure 5 for the AAIW layer. The grey circles and black crosses in both panels are CTD profiles collected during the CLIVAR/WOCE A10 (~30°S) and CITHER-2 LEG 1 (WOCE A17, 45–48°S) sections, respectively. The inset in (a) shows the θ-S distribution along the western boundary from Argo data at three selected latitude ranges: 34–31.5°S (blue), 31.5–29°S (black), and 29–27.5°S (red). The heavy lines (shading) are the profile averages (standard deviation). The red dashed rectangle in (a) indicates boundaries of the inset. See Figure 1 for CTD stations and Argo profiles location.

(167, 125, and 55, respectively), the significantly higher salinity standard deviation about θ at the 34.5°S–31.5°S range further suggests the presence of a wider range of AAIW varieties closer to the SAMBA-W line than is found farther north.

Because the AAIW recirculating with the subtropical gyre is continually eroded by mixing with adjacent water masses (i.e., SACW and UCDW), thereby increasing its salinity and decreasing its oxygen concentration, the properties observed in the eastern half of the SAMBA-W line indicate the presence of more pristine varieties of AAIW from farther south. The source of these waters must be the more recently ventilated AAIW derived from the northern Drake Passage and advected northward along the Subantarctic Front by the MC, as indicated by the properties of the waters observed near the Malvinas Escarpment at this density range. Hence, we hypothesize that the old (lower in O_2 concentration), recirculated AAIW flowing south underneath the BC mixes with recently formed AAIW in the BMC and returns north below the BC offshore recirculation. The July 2012 snapshot (Figure 2d) and the averaged (Figure 3d) velocity sections are in agreement with this result, displaying a southwest flow of ~10–15 cm/s west of 49°W and a weaker return flow farther offshore. Moreover, we suggest that this recirculation cell extends at least as far north as 27°S. This is confirmed by the Argo floats nearby the western boundary: the southward salinity decrease observed between the Santos Bifurcation and the SAMBA-W line can only be accounted for by a continuous injection of recently ventilated AAIW from the BMC.

4.1.4. Upper Circumpolar Deep Water

The UCDW is the upper branch of the Circumpolar Deep Water (CDW), a large body of relatively fresh and oxygen-poor water within the Southern Ocean that arises from the mixing of upwelled NADW with waters circulating within the Antarctic Circumpolar Current (Reid et al., 1977). As CDW is reinjected into the South Atlantic along the western edge of the Argentine Basin within the MC, the southward flowing NADW, which shares a similar density range, splits it into an upper (UCDW) and a lower (LCDW) branch (Mémery et al., 2000; Reid et al., 1977). At the SAMBA-W line, however, the average isopycnal surfaces within the UCDW suggest a mean poleward flow at the western end as observed in the AAIW layer (Figure 3). The potential temperature range within the UCDW at 34.5°S is relatively narrow (2.65 °C $< \theta <$ 3.62 °C), and the core is characterized by a sharp oxygen minimum (O_2 ~ 190 μmol/kg; Figure 4b and Table 2). Synoptic sections consistently show that the potential temperature and the dissolved oxygen concentration at the UCDW core monotonically decrease in the offshore direction at the SAMBA-W line (e.g., Figure 2). The average θ-S and θ-O_2 distributions at this latitude depicted in Figure 7 show that close to the slope (at 51.5°W), the upper fraction of UCDW

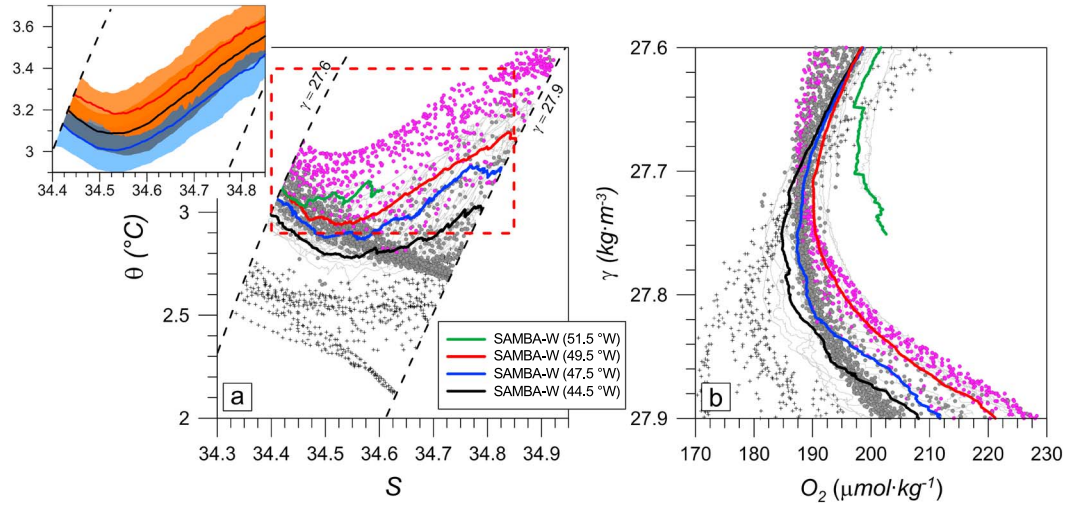

Figure 7. (a and b) Same as Figure 5 for the UCDW layer except (b) is a γ versus O_2 distribution. The magenta (grey) circles in both panels are CTD profiles collected within (farther than) 500 km of the 200 m isobath at the CLIVAR/WOCE A10 sections (~30°S), and the black crosses are CTD profiles collected at the CITHER-2 LEG 1 (WOCE A17, 45–48°S) section. The inset in (a) shows the θ-S distribution along the western boundary from Argo data at three selected latitude ranges: 34–31.5°S (blue), 31.5–29°S (black), and 29–27.5°S (red). The heavy lines (shading) are the profile averages (standard deviation). The red dashed rectangle in (a) indicates boundaries of the inset. See Figure 1 for CTD stations and Argo profiles location.

($S < 34.6$) is significantly different than further offshore, on average warmer ($\theta > 3$ °C) and more oxygenated ($O_2 > 200$ μmol/kg; green line in Figures 7a and 7b). This is most likely a combination of two effects: (i) near-bottom intensification of diapycnal mixing with the overlying O_2 rich AAIW and (ii) the southward recirculation along the western boundary, which allows more time for mixing. By contrast, the lower portion of UCDW ($S > 34.6$, $\gamma > 27.75$ kg/m^3) is modified due to the somewhat more subtle differences between the NADW varieties flowing underneath. At 49.5°W, the potential temperature increases from 2.92 °C at S ~ 34.52 to 3.35 °C at S ~ 34.83 due to interaction with the relatively warmer NADW flowing southward within the DWBC (red line in Figure 7a). By contrast, θ increases roughly half as much in the same salinity range on the eastern end of the section because of the relatively colder variety of NADW found there (black line in Figure 7a). Argo profiles collected between 34.5°S and 27°S close to the slope show a monotonic northward temperature increase (inset in Figure 7a), suggesting a recirculation cell that extends farther north, similar to that discussed above for the AAIW layer. Inspection of θ-S properties from CTD profiles collected near 30°S further supports this hypothesis. For this data set, it is useful to discriminate the profiles collected close to the continental slope (i.e., within 500 km in the cross-shore direction from the 200 m isobath; magenta circles in Figure 7) from those collected farther offshore (i.e., farther than 500 km from the 200 m isobath; grey circles in Figure 7). The UCDW close to the slope is significantly warmer ($\theta > 3.2$ °C) and more oxygenated at $\gamma > 27.8$ kg/m^3 due to mixing with the relatively warm and oxygen-rich variety of NADW flowing underneath, while that observed offshore presents potential temperatures within the range found at the SAMBA-W line.

Unlike the AAIW, once the UCDW leaves its "source" region in the Southern Ocean and recirculates through the South Atlantic, its oxygen concentration increases with time due to mixing with the adjacent and relatively more oxygenated AAIW and NADW. Therefore, the overall temperature and oxygen decreasing in the offshore direction observed at the SAMBA-W line requires admixtures with more "pristine" varieties of UCDW, such as those found near the Malvinas Escarpment (crosses in Figure 7). The recirculation pattern of UCDW in the vicinity of the SAMBA-W line thus resembles that of the AAIW layer, with older, recirculated UCDW flowing southward across 34.5°S as a slope current underneath the BC, mixing at the BMC with more pristine UCDW advected northward by the MC, and then recirculating northward beneath the BC offshore recirculation. As with the AAIW, the July 2012 alongshore velocity section and the averaged section also corroborate this circulation pattern for the UCDW (Figure 2d and 3d). The averaged section, however, displays a weaker northward flow of ~5 cm/s at 47°W.

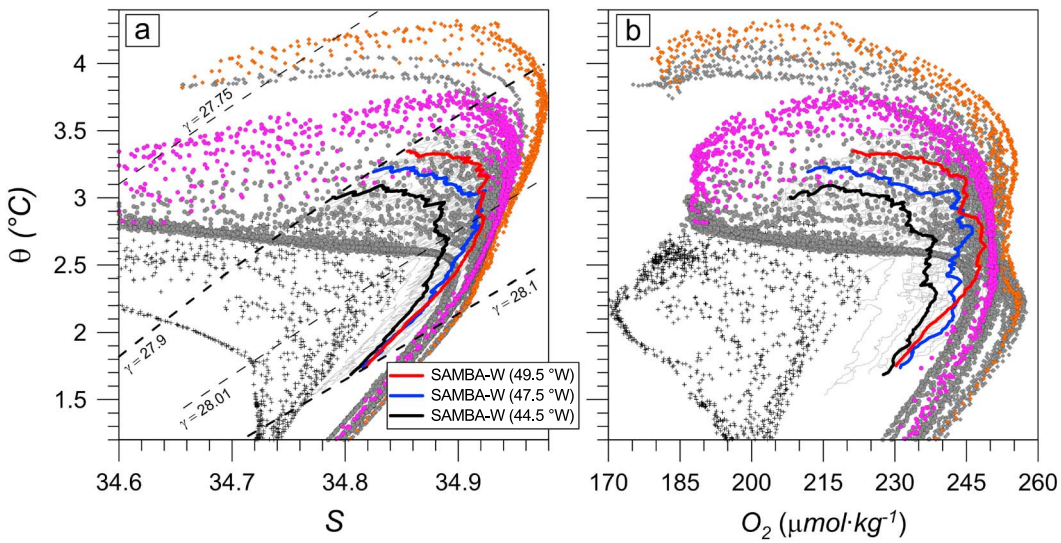

Figure 8. Same as Figure 5 for the NADW layer. The orange (grey) diamonds are CTD profiles collected within (farther than) 300 km of the 200 m isobath at the CITHER-2 LEG 2 section (13°S); the magenta (grey) circles are CTD profiles collected within (farther than) 200 km of the 200 m isobath at the CLIVAR/WOCE A10 (~30°S); the black crosses are CTD profiles collected during the CITHER-2 LEG 1 (WOCE A17, 45–48°S) section. The CTD data collected at the SAMBA-W line are bounded to the NADW γ limits; all other data are limited to $\gamma > 27.7$ kg/m^3. See Figure 1 for CTD stations locations.

4.1.5. North Atlantic Deep Water

The DWBC at the SAMBA-W line is mainly composed of recently ventilated NADW, which is clearly identifiable by its high oxygen concentration ($O_2 > 240$ μmol/kg), relatively high potential temperature (2.0 °C $< \theta <$ 3.5 °C) and high salinity ($S > 34.8$; Figures 2 and 3a–3c and Table 2). However, the θ, S, and O_2 maxima within the NADW as observed in the synoptic sections are offset vertically, indicating slightly different NADW types (e.g., Figure 2). The warmest variety of NADW is concentrated against the bottom slope just below the interface with UCDW ($\theta > 3.3$, Figure 2a), and the NADW substantially cools in the offshore direction, whereas the average salinity (S ~ 34.95, γ = 27.985 kg/m^3) and oxygen (O_2 ~ 250 μmol/kg^1, γ = 27.995 kg/m^3) maxima are located at a higher neutral density levels. Farther north, in the western tropical South Atlantic, the NADW is commonly divided into three sublayers, namely, Upper (uNADW), Middle (mNADW), and Lower NADW (lNADW), identified by a shallow salinity maximum and two deep oxygen maxima, respectively (Mémery et al., 2000; Tsuchiya et al., 1994). In what follows, before analyzing the NADW properties at 34.5°S, we will describe how these sublayers are modified as the NADW flows southward along the boundary. This will provide the basin-scale perspective required to interpret our observations at the SAMBA-W line.

At 13°S, the core of uNADW is characterized by a salinity maximum higher than 34.97 and θ ~ 3.75 °C near the continental boundary (orange diamonds in Figure 8a), whereas it is somewhat fresher, colder, and less oxygenated farther offshore (θ ~ 3.60 °C, S ~ 34.96; grey diamonds in Figure 8a). This maximum salinity layer is capped by still warmer but fresher waters that must be a variety of NADW due to their high potential temperature, but nonetheless lie outside our defined NADW neutral density limits ($\theta > 3.7$ °C, S ~ 34.90, 27.75 kg/m^3 $< \gamma <$ 27.90 kg/m^3). The water mass overlying the uNADW is also associated with high tritium and chlorofluorocarbons (not shown) and is referred to in literature as *shallow* uNADW (suNADW; Rhein et al., 1995). Note that warmer waters ($\theta > 4.1$ °C) are also found against the continental boundary in this neutral density range (Figure 8a). Interestingly, the oxygen concentration at this θ maximum is significantly lower (195 μmol/kg $< O_2 <$ 215 μmol/kg; orange diamonds in Figure 8b) than at the underlying NADW. Because the UCDW does not reach as far north as 13°S (Tsuchiya et al., 1994), we associate the relatively warm, oxygen-poor suNADW with a modified variety of uNADW derived from a direct mixture between the uNADW and the lower portion of the AAIW, which is characterized by low O_2 concentration (140 μmol/kg $< O_2 <$ 160 μmol/kg) in the vicinity of 13°S (Tsuchiya et al., 1994). We will examine the θ maximum associated with the suNADW farther south because it has an important role in modifying the UCDW/NADW

interface in the vicinity of the SAMBA-W line. The deepest levels within NADW (28.01 kg/m^3 $< \gamma <$ 28.10 kg/m^3) at 13°S are occupied by the mNADW and lNADW, which are characterized by two oxygen maxima located at θ ~ 3.5 °C, O_2 ~ 250 μmol/kg and at θ ~ 2.2 °C, O_2 ~ 255 μmol/kg, respectively (Figure 8b).

At ~30°S, the uNADW is colder and fresher than at 13°S but is still recognizable by a salinity maximum, particularly close to the boundary (θ ~ 3.4 °C, $S >$ 34.94; magenta circles in Figure 8a). The potential temperature maximum associated with suNADW is also present right above the salinity maximum and is colder and slightly fresher than farther north. As observed at 13°S, there is also a marked temperature difference at the θ maximum between waters found close to the slope (θ ~ 3.7 °C, 34.86 $< S <$ 34.92; magenta circles in Figure 8a) and offshore (2.9 °C $< \theta <$ 3.3 °C, 34.86 $< S <$ 34.92; gray circles in Figure 8a). The profiles collected east of the Rio Grande Rise (~33°W) show no trace of the potential temperature maximum. Rather, there is a monotonic cooling and a salinity and oxygen concentration increasing with greater depth between the UCDW at $\gamma <$ 27.9 kg/m^3 and the inflection point at θ = 2.4 °C, S = 34.9, and O_2 = 247 μmol/kg. Below this level, the O_2 extremes in the mNADW and lNADW sublayers are smoother as a result of mixing as the DWBC flows southward throughout the section. Close to boundary, the oxygen maximum associated with lNADW is noticeable at θ ~ 2.45 °C, O_2 ~ 250 μmol/kg; these values are about 0.25 °C warmer and 5 μmol/kg less oxygenated than those observed at 13°S. By contrast, the O_2 maximum associated with mNADW is manifested as an inflection point centered at θ ~ 3.3 °C and O_2 ~ 246 μmol/kg. Offshore of the Rio Grande Rise, the NADW at 28.01 kg/m^3 $< \gamma <$ 28.1 kg/m^3 is about 0.05 fresher and 5 μmol/kg less oxygenated (Figure 8b).

At the SAMBA-W line, the distinct characteristics of uNADW, mNADW, and lNADW vanish almost completely. The averaged θ-S and θ-O_2 diagrams exhibit a single, smooth inflection point at the NADW core, which becomes increasingly eroded in the offshore direction. At 49.5°W, the salinity maximum that could be traced as uNADW ($S >$ 34.92) is located at a lower neutral density range (27.96 kg/m^3 $< \gamma <$ 28.02 kg/m^3) than the uNADW found farther north close to the slope. It is also associated with a secondary O_2 maximum, a remnant of mNADW with concentrations not exceeding 245 μmol/kg at θ = 3.15 °C (red curve in Figure 8b). By contrast, the oxygen maximum associated with the lNADW vanishes through mixing with the underlying LCDW. As a result, the deepest oxygen maximum observed at 49.5°W is located at a lower density and is warmer and less oxygenated than the deepest oxygen minimum observed farther north (O_2 = 247 μmol/kg, 2.4 °C $< \theta <$ 2.8 °C, 28.02 kg/m^3 $< \gamma <$ 28.05 kg/m^3; Figures 8a and 8b). Furthermore, the warm layer associated with suNADW is still present close to boundary ($\theta >$ 3.3 °C in Figure 3a). The interface between UCDW and NADW in the western boundary of the SAMBA-W line is not well defined because the density of the warm suNADW is similar to the UCDW (Mémery et al., 2000) and they are both poorly oxygenated due to mixing with the overlying low oxygen waters from the tropical region. Indeed, the average potential temperature maximum at 49.5°W within this warm layer is found at θ = 3.387 °C, γ = 27.884 kg/m^3, that is, within the UCDW density range (red curve in Figure 7a). Hence, using γ = 27.9 kg/m^3 as the UCDW/NADW interface will inevitably label the warm suNADW generally found close to the continental slope as UCDW. Although these waters are too warm for the traditional definition of UCDW, we decided to keep γ = 27.9 kg/m^3 as the NADW upper limit throughout the entire section because it effectively keeps most of the highly oxygenated waters within NADW limits (see, for example, the synoptic section in Figure 2).

At the eastern end of the SAMBA-W line, at 44.5°W, the NADW is overall colder ($\theta <$ 3 °C), fresher ($S <$ 34.89), and less oxygenated ($O_2 <$ 240 μmol/kg; black curve in Figures 8a and 8b), clearly evidencing the eroded nature of the NADW found offshore. The averaged θ-S and θ-O_2 properties at the deepest portion of the NADW ($\theta <$ 2 °C) converge at all selected longitudes, and the oxygen concentration significantly decreases downward due to mixing with the underlying LCDW. By contrast, at ~30°S and 13°S, the O_2 decreases almost linearly with temperature from its maximum at the lNADW core to values associated with AABW (circles and diamonds in Figure 8b), evidencing the absence of LCDW at these latitudes.

In agreement with Mémery et al. (2000), who set the deep front between the uNADW and UCDW approximately at 26°S, our results indicate that at ~30°S as well as at 34.5°S, θ does not exceed ~3.7 °C within the layer defined by 27.75 kg/m^3 $< \gamma <$ 27.90 kg/m^3 (Figures 7a and 8a), thus implying that south of ~30°S and away from the slope, this density range is occupied by UCDW. However, our results also reveal the presence of an intensified southward flow against the slope between 13°S and the SAMBA-W line, which conveys a relatively warm but poorly oxygenated variety of uNADW that we associate with suNADW.

As it spreads away from the DWBC into the interior, the NADW mixes with adjacent water masses, thus becoming colder, fresher, and less oxygenated. As a result, observations at 13°S and 30°S show that recently ventilated NADW is found near the slope whereas older, eroded varieties are found farther offshore (Figure 8). However, at the SAMBA-W line, this difference is larger; that is, the NADW variety found offshore is significantly more eroded at 34.5°S than farther north, particularly at neutral densities higher than 28.01 kg/m^3 (Figure 8a). There are two potential pathways that could explain these observations:(i) the diluted NADW found east of ~43°W at 27°S flows southward across this latitude and reaches 34.5°S intensifying its erosion rate as it mixes with the more concentrated UCDW and LCDW located in the vicinity of the SAMBA-W line and (ii) there is a recirculation cell, which conveys a diluted variety of NADW from south of the SAMBA-W line. The latter hypothesis has been also suggested by Meinen et al. (2012) on the basis of oxygen measurements from the SAM05 cruise (July 2011). More recently, Meinen et al. (2017) used PIES measurements collected between 2009 and 2014 to show that the DWBC east of 49.5°W has on average a northward component across the SAMBA-W line. The weak upward slope in the offshore direction of the time-averaged isopycnals east of 47°W provides further evidence supporting this hypothesis (Figure 3). Direct velocity measurements from LADCP show a southwestward flow against the slope reaching an average maximum of 15 cm/s at 49°W and a somewhat weaker return flow of 5–10 cm/s in the vicinity of 47°W (Figures 2d and 3d). We therefore accept the second pathway as the most likely for the recirculated NADW.

The NADW found in the offshore portion of the SAMBA-W line is overall more eroded than that found at 30°S (black line and grey circles in Figure 8a, respectively), particularly at $\gamma > 28.01$ kg/m^3, meaning that the recirculated NADW flowing northward across the SAMBA-W line could not feed the diluted varieties found at 30°S. This observation suggests that the recirculated NADW flowing northward across 34.5°S must be driven away from the western boundary toward the interior of the basin between 34.5 and 30°S**.** This eastward spreading is in agreement with the numerical model analysis of van Sebille et al. (2012), who found 1 Sv of NADW crossing eastward along a quasi-zonal secondary pathway at 32°S.

4.1.6. Lower Circumpolar Deep Water/Antarctic Bottom Water

Beneath the NADW, the abyssal layer at the SAMBA-W line is occupied by LCDW and AABW. The coldest and densest water mass is the AABW, which is mainly composed of Weddell Sea Deep Water (WSDW). This is the youngest abyssal water mass escaping the Southern Ocean (Orsi et al., 1999), hence its relatively high oxygen ($O_2 > 225$ μmol/kg, Figure 4b). The Antarctic origin of the AABW explains its cold nature, which is the reason why the 0 °C isotherm is a commonly used criterion to separate AABW from LCDW (Georgi, 1981a; Preu et al., 2013). Indeed, the γ = 28.27 kg/m^3 isopycnal closely follows the 0 °C isotherm along the SAMBA-W line (e.g., Figure 2). The overlying LCDW is on average more oxygenated than the UCDW (θ = 0.7 °C, O_2 ~ 215 μmol/kg; Figure 4) due to mixing with the WSDW. Unlike in the overlying layers, the properties in the LCDW/AABW density range ($\gamma > 28.10$ kg/m^3) are largely homogeneous along the SAMBA-W line (Figures 2 and 3), which suggests the absence of opposing flows near the western boundary at this latitude. In what follows, we will evaluate how the LCDW and the AABW are modified as they are spread into the South Atlantic from the Malvinas Escarpment downstream to the northern Argentine Basin across the SAMBA-W line.

As indicated by Arhan et al. (1999), individual CTD profiles collected near the slope at ~48°S show LCDW flowing northward with the deep MC (~2,600–4,400 m). The influence of NADW in this region is minor and restricted to waters with $\theta > 1.20$ °C (black crosses in Figure 9a). These observations show a relatively fresh layer between 0.90 °C $< \theta <$ 1.80 °C, which is characterized by constant salinity (S ~ 34.72). Immediately above this layer, the potential temperature decreases and the salinity increases monotonically with greater depth between 27.60 kg/m^3 $< \gamma <$ 28.01 kg/m^3, thus indicating a direct mixture of LCDW and UCDW in this density range (Figures 7a and 8a). The absence of NADW is also evident in the θ-O_2 relationship, where oxygen decreases upward linearly with increasing temperature from the relatively high AABW values ($\theta \sim -0.15$ °C, O_2 ~ 225 μmol/kg, Figure 9b) to a minimum at the UCDW core (θ ~ 2.20 °C, O_2 ~ 170 μmol/kg, Figure 8b). By contrast, the LCDW is capped by NADW farther offshore, causing a monotonic salinity increase at $\theta > 0.7$ °C and an oxygen minimum at θ ~ 1.30 °C (grey crosses in Figures 9a and 9b). Along the SAMBA-W line, the oxygen minimum associated with LCDW at the three selected longitudes is on average higher and colder (θ ~ 0.75 °C, O_2 ~ 216 μmol/kg) than across the Malvinas Escarpment, thus indicating substantial erosion by diapycnal mixing as well as isopycnal mixing with NADW in an equal density range as these waters flow along the western boundary of the Argentine Basin.

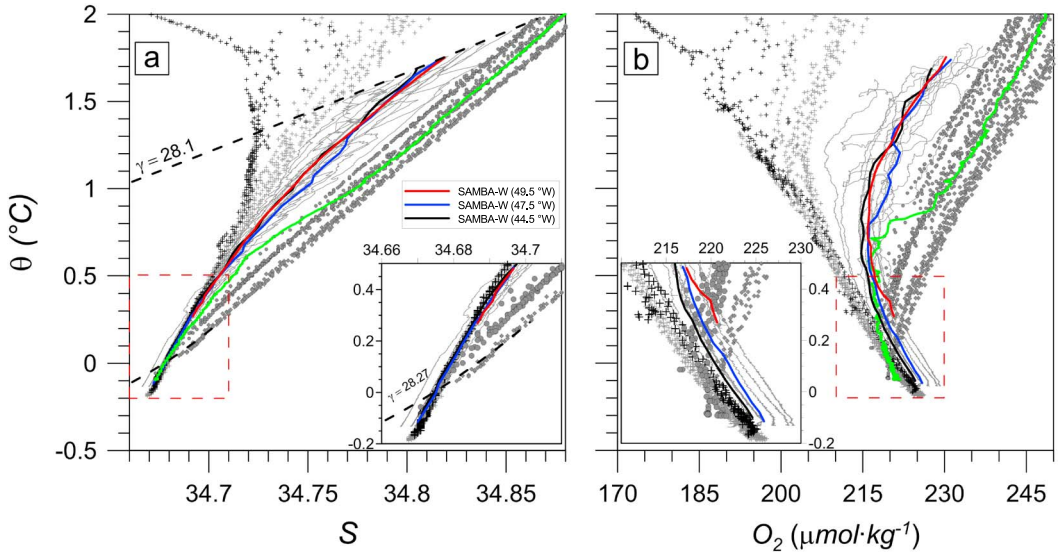

Figure 9. Same as Figure 5 for the LCDW/AABW layer. The black (grey) crosses in both panels are CTD profiles collected within (farther than) 200 km of the 200 m isobath at the CITHER-2 LEG 1 (WOCE A17, 45–48°S) section. The circles and diamonds are CTD stations occupied at the CLIVAR/WOCE A10 (~30°S) and the CITHER-2 LEG 2 (13°S) sections, respectively. The green curve is an individual CTD station collected during the 2011 WOCE A10 section at the Vema Channel near 39.4°W, 30°S. The bottom layer is expanded in the insets. See Figure 1 for CTD stations locations.

At 30°S there is no trace of LCDW at $\gamma < 28.22$ kg/m^3 ($\theta > 0.4$ °C) except for an individual CTD profile collected at the Vema Channel (~39.4°W) during the 2011 WOCE A10 section. This profile reveals the presence of LCDW somewhat saltier than those found at the SAMBA-W line but with very similar O_2 concentrations at $\theta < 0.9$ °C (green line in Figure 9). Except for this individual profile, there is an indication of direct mixing between lNADW ($\theta \sim 2.0$ °C, $O_2 \sim 250$ μmol/kg) and the densest portion of LCDW ($\theta < 0.4$ °C, $O_2 < 220$ μmol/kg), manifested by a monotonic temperature, salinity, and oxygen concentration decreasing with greater depth. At $\theta < 0.4$ °C, however, the oxygen concentration is similar to that observed at the SAMBA-W line. An inflection in the θ-O_2 curve at $\theta \sim 0.2$ °C, $O_2 \sim 185$ μmol/kg further suggests mixing with the underlying AABW at 30°S (grey circles, inset in Figure 9b).

The oxygen concentrations at $\theta < 0.050$ °C are similar to those observed at the Malvinas Escarpment (~220 μmol/kg). However, the O_2 in this temperature range is on average ~3–5 μmol/kg higher at the SAMBA-W line. This is caused by three anomalous profiles collected during the SAM05 and SAM07 cruises. Only two bottle samples within the AABW are available to verify these values. Unfortunately, the differences between the CTD measurements and the bottle samples are too large (15 and 5 μmol/kg) to determine if these casts reveal a real increase in dissolved oxygen concentration in AABW in recent years. Farther north, observations show no trace of LCDW as well. A significantly warmer and saltier variety of AABW is found at 13°S ($0.040 < \theta < 0.075$, $34.685 < S < 34.698$; inset in Figure 9a), and the absence of inflections in the θ-O_2 curve further suggests an admixture of lNADW and AABW at $\gamma > 28.1$ kg/m^3, without the presence of LCDW at all.

LCDW and AABW spread into the Argentine Basin from the Drake Passage and around the South Sandwich Trench closely following the western edge of the basin as a DWBC beneath the deep MC (Georgi, 1981a; Reid, 1989; Figure 1a). Based on hydrographic observations, Coles et al. (1996) have suggested a bifurcation of the abyssal flow at the BMC, with a branch flowing northward along the western boundary and the other branch recirculating poleward through the interior of the basin. The latter branch somewhat resembles the flow of the MC, which retroflects southward at the BMC. This is consistent with the hydrographic observations collected near the Malvinas Escarpment, which show more pristine LCDW near the slope and a diluted variety farther offshore (Figure 9). Previous studies (Georgi, 1981a; Speer & Zenk, 1993) indicate a cyclonic circulation of LCDW and AABW in the northwest Argentine Basin, that is, northeastward across the SAMBA-W line. In agreement with observations from Reid et al. (1977), the time-mean isopycnal surfaces in the SAMBA-W line slope upward toward the west (Figure 3), also suggesting a downward increase of the northward flow. The

Table 3
Average Potential Temperature (θ, °C), Salinity (S), and Dissolved Oxygen Concentration (O_2, μmol/kg) for Each Representative Neutral Density (γ, kg/m^3) Range at Four Selected Longitudes Along the SAMBA-W Line Computed Using CTD Profiles Collected Between 2009 and 2012

	51.5°W			49.5°W			47.5°W			44.5°W		
γ range	θ	S	O_2	θ	S	O_2	θ	S	O_2	θ	S	O_2
25.60–26.50	18.134 (0.417)	36.036 (0.139)	212 (12)	18.043 (0.268)	36.000 (0.086)	223 (7)	17.775 (0.357)	35.911 (0.116)	229 (7)	17.487 (1.001)	35.822 (0.321)	229 (15)
26.60–27.10	10.526 (0.232)	34.896 (0.053)	211 (5)	10.497 (0.183)	34.889 (0.043)	214 (5)	10.422 (0.214)	34.872 (0.050)	217 (4)	10.316 (0.283)	34.850 (0.063)	218 (5)
27.20–27.40	4.711 (0.286)	34.288 (0.047)	236 (12)	4.551 (0.297)	34.260 (0.050)	239 (13)	4.394 (0.182)	34.235 (0.030)	250 (5)	4.382 (0.126)	34.233 (0.020)	246 (7)
27.55–27.65	3.127 (0.132)	34.420 (0.021)	202 (4)	3.121 (0.068)	34.419 (0.011)	199 (1)	3.072 (0.090)	34.411 (0.014)	199 (2)	2.989 (0.041)	34.397 (0.007)	199 (2)
27.85–27.95	–	–	–	3.322 (0.202)	34.852 (0.039)	222 (9)	3.196 (0.240)	34.827 (0.045)	214 (10)	3.005 (0.174)	34.790 (0.033)	209 (7)
27.95–28.05	–	–	–	2.911 (0.104)	34.918 (0.022)	245 (7)	2.862 (0.099)	34.907 (0.021)	240 (6)	2.736 (0.165)	34.880 (0.034)	234 (11)
28.10–28.20	–	–	–	1.106 (0.029)	34.753 (0.006)	220 (2)	1.129 (0.068)	34.758 (0.014)	221 (4)	1.104 (0.080)	34.752 (0.017)	219 (7)

Note. The standard deviation of the observed values within each neutral surface layer is indicated in brackets. The deep dense layers that are never observed at the shallower westernmost longitude are each denoted by a dash.

LADCP observations show a weak southward flow (just over 5 cm/s) within the LCDW range and east of 47.5°W that contrasts with the average northward flow derived from our water mass analysis. Whether this disparity is due to the low accuracy of the LADCP in this deep, low-scattering environment is difficult to assess with the available data. Future observations will be required to better assess the circulation at this level. Regardless, our water mass analysis shows that the upper portion of the LCDW found at the SAMBA-W line ($\theta > 0.9$ °C) does not actually reach 30°S, thus indicating an average eastward spreading between this latitude and 34.5°S. Based on hydrographic and CFC data collected during the WOCE section A17, Mémery et al. (2000) also found evidence of an eastward turning of the LCDW at ~34.5°S. CTD profiles collected along this section clearly show a deep front located approximately at 28.10 kg/m^3 $< \gamma <$ 28.25 kg/m^3, which separates the less oxygenated and relatively fresh LCDW to the south from an admixture of NADW and AABW to the north (not shown). Our results also indicate that the densest fraction of the LCDW ($\theta < 0.2$ °C, $\gamma > 28.25$ kg/m^3) continues northward and outflows into the Brazil Basin through the Vema Channel, ultimately mixing with the underlying AABW. Therefore, these results indicate that the upper LCDW turns eastward after colliding with the southward flowing NADW.

Our water mass analysis suggests an average northward flow of AABW across the SAMBA-W line. In agreement with this result, the velocity estimates from the PIES array also show an average northward flow of AABW between 47.5°W and 44.5°W during 2009–2014 (Meinen et al., 2017). By contrast, if these estimates are averaged over the 2012–2014 time span, the AABW flow is southward in the offshore portion of the SAMBA-W line. Bottom track velocities derived from the LADCP measurements show the AABW flow close to the bottom (~100–120 m above the seafloor) switching between a northeastward to a southwestward direction between realizations (not shown). These opposite results thus suggest that the meridional flow of AABW may reverse and stress the importance of collecting long-term absolute velocity measurement in the abyssal layers.

4.2. Water Mass Variability

In this section we investigate the temporal changes of the water mass properties along the SAMBA-W line between successive hydrographic sections. The sections of the standard deviation of θ, S, and O_2 relative to the time averages yield a comprehensive view of the temporal variability of the water mass properties (Figures 3d–3f). To further study the zonal structure of this variability, the standard deviation of θ, S, and O_2 relative to the average profiles at four selected longitudes is computed as explained in section 2. To effectively remove local sources of variability, such as evaporation/precipitation or the passage of synoptic weather systems, property changes in the upper 50 m are excluded from the analysis. The results are focused on neutral density layers and presented in Table 3. Because only two austral spring/summer sections are available, it is not possible to isolate and study the seasonal variability of the water mass properties with CTD sections only. We explored all the Argo data collected in the vicinity of the SAMBA-W line to further analyze a potential seasonal signal. However, we found that due to the uneven spatial and temporal distribution and the nonsynoptic nature of these data, the variability among profiles collected within an individual season is higher than any

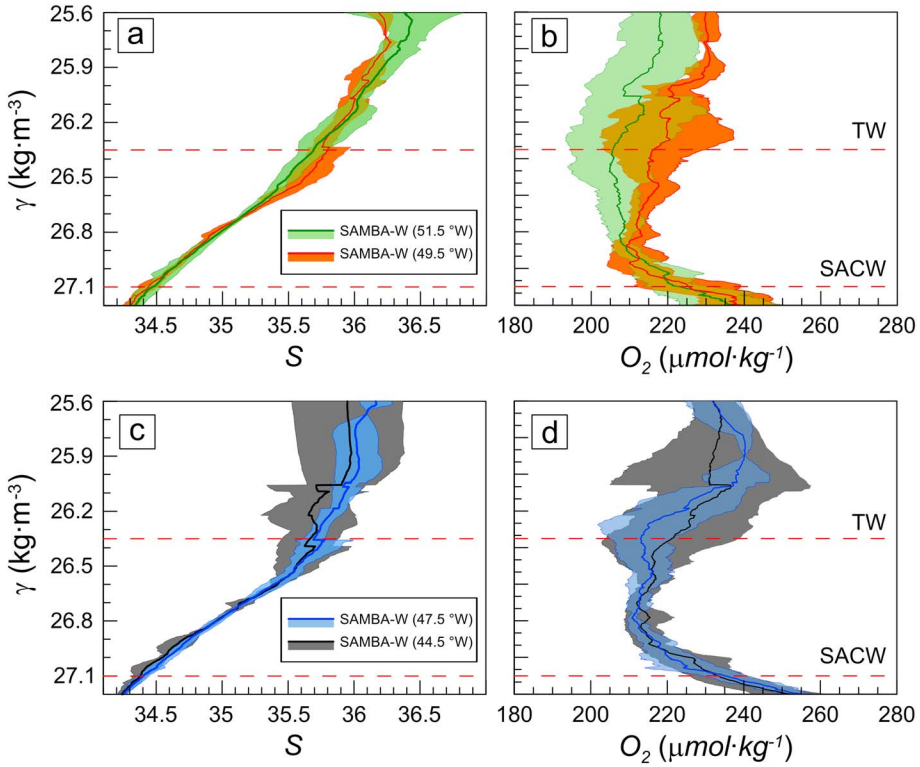

Figure 10. Time-mean profiles of (a and c) S and (b and d) O_2 computed along neutral density (γ) surfaces for the upper layer at four selected longitudes along the SAMBA-W line. The shading in all panels indicates the standard deviation for each density level. The red dashed lines are the γ surfaces used to delimit each water mass. The water mass layers are indicated in (b) and (d).

noticeable difference associated with a seasonal cycle. Therefore, we do not attempt to thoroughly study any aspects of the seasonality of the standard deviations in what follows. In addition, because changes in the AABW are just above the measurement accuracy levels, a more thorough analysis for this layer is left to a future study.

The time-mean salinity and dissolved oxygen concentration profiles along with their standard deviations for the upper portion of the water column are presented in Figure 10. The largest θ, S, and O_2 standard deviations are observed in the TW core and its interface with the SACW (25.60 kg/m^3 $< \gamma <$ 26.50 kg/m^3; see also Table 3). The standard deviation profiles also show that the variability in this density range is generally higher at both ends of the SAMBA-W line. Close to the continental slope, at 51.5°W (green line in Figures 10a and 10b), the high standard deviation in salinity at $\gamma <$ 25.70 kg/m^3 is due to the difference between the significantly warm and salty TW advected southward by the BC during the austral summer and the relatively fresher waters observed during winter time. On the other hand, the largest temperature and salinity changes at the eastern end of the section (44.5°W, black line in Figures 10c and 10d; $\gamma \sim$ 26.00 kg/m^3) are associated with the presence of the relatively cold and fresh subantarctic waters. This also explains why the lightest fraction of the TW ($\gamma <$ 26.00 kg/m^3) is on average 0.3 fresher at 44.5°W than at 51.5°W. By contrast, the lower half of the SACW (26.60 kg/m^3 $< \gamma <$ 27.10 kg/m^3) is characterized by a band of low variability in θ, S, and O_2 at all four selected longitudes along the SAMBA-W line (Figures 3d–3f and 10). Indeed, the standard deviation in this density range is about half of that observed in the overlying layers (Table 3). These denser SACW are too deep to be influenced by deep winter convection associated with mode water formation (Sato & Polito, 2014).

The time-mean and standard deviation of S and O_2 at the intermediate levels at each selected longitude along the SAMBA-W line are presented in Figure 11. The highest variability is observed at the core of the AAIW at 51.5°W and 49.5°W (see also Figures 3a and 3b and Table 3). Inspection of the individual hydrographic sections shows the occurrence of events when anomalously fresh and highly oxygenated AAIW in the 27.20 kg/m^3 $< \gamma <$ 27.40 kg/m^3 range are found in this portion of the section. Compare, for example,

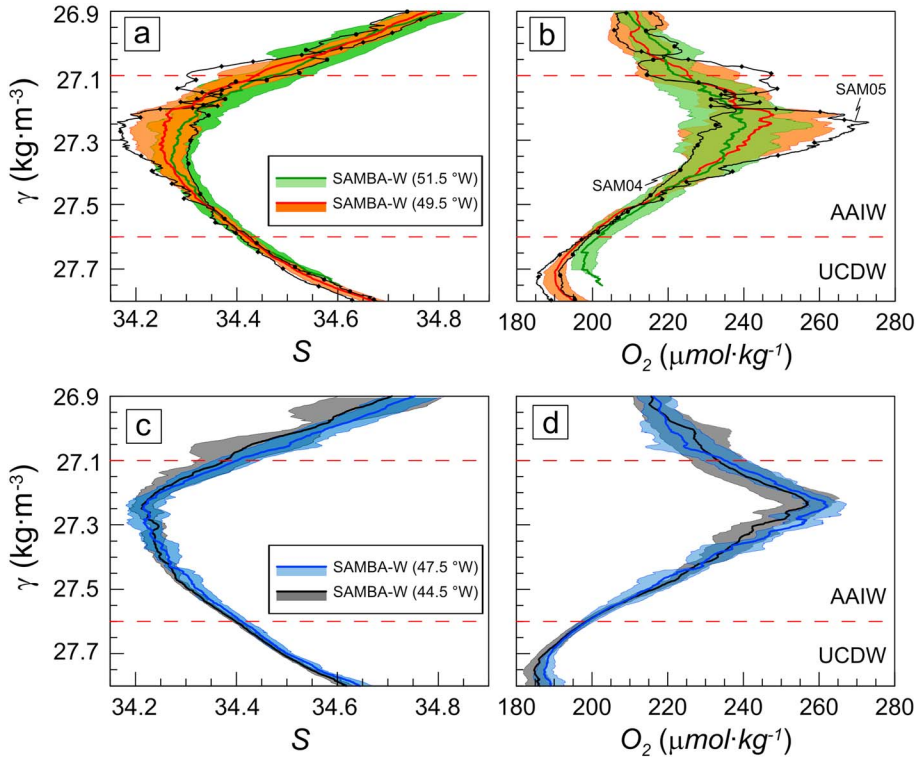

Figure 11. Same as Figure 10 for the intermediate layer. Two individual CTD profiles collected at 49.5°W during SAM04 (December 2010) and SAM05 (July 2011) cruises are shown in black in (a) and (b).

two CTD stations occupied at 49.5°W during SAM04 (December 2010) and SAM05 (July 2011; black thin lines in Figures 11a and 11b). The freshest and most oxygenated variety of AAIW ($S < 34.2$, $O_2 > 270$ μmol/kg at $\gamma \sim 27.25$ kg/m^3) was observed during the latter occupation, whereas an eroded AAIW was found during the former cruise ($S > 34.3$, $O_2 < 230$ μmol/kg at $\gamma = 27.30$ kg/m^3). By contrast, the properties of the relatively low salinity and oxygen-rich variety of AAIW observed offshore from the BC, at 47.5°W and 44.5°W, are significantly less variable (Figures 11c and 11d and Table 3). Below the AAIW core, the AAIW/UCDW interface is characterized by a band of minimum variability throughout the entire SAMBA-W line, except over the continental slope. The θ, S, and O_2 standard deviations at 49.5°W, 47.5°W, and 44.5°W in the 27.55 kg/m^3 $< \gamma <$ 27.65 kg/m^3 range are approximately a third of that at the AAIW core, whereas these values are significantly larger at 51.5°W (Table 3).

The time-mean and standard deviation of S and O_2 at the deep and abyssal levels at 49.5°W and 44.5°W are presented in Figure 12. The variability at the NADW layer increases toward the eastern end of the SAMBA-W line (Figures 3d–3f). As discussed above, the offshore portion of the section is generally occupied by eroded, older NADW, and thus, the salinity and dissolved oxygen concentration at its core is on average lower at 44.5°W than at 49.5°W (black and red curves, Figure 12). However, more pristine (higher S and O_2) varieties of NADW are sporadically observed circulating in this region, thus generating higher variability there. For example, in the 27.95 kg/m^3 $< \gamma <$ 28.05 kg/m^3 range, the S standard deviation is 0.022 at 49.5°W and 0.034 at 44.5°W (Table 3). To illustrate these types of events, two CTD profiles collected at 44.5°W SAM04 (December 2010) and SAM08 (December 2012) are also plotted in Figure 12 (blue lines). Note the marked difference between the less eroded core of NADW observed in 2010 compared to that found in 2012. The former presents higher salinity (S $>$ 34.9) and dissolved oxygen concentrations ($O_2 > 250$ μmol/kg), clearly indicating the presence of younger NADW at the eastern end of the section, whereas the latter is significantly fresher (S ~ 34.875), less oxygenated ($O_2 \sim 235$ μmol/kg) and presents ubiquitous small-scale interleaving, characteristic of the recirculated variety of NADW.

Within the BC offshore recirculation, variations in salinity and dissolved oxygen concentration in the upper 200 m are consistent with the energetic mesoscale activity that characterizes the region (Figure 1b).

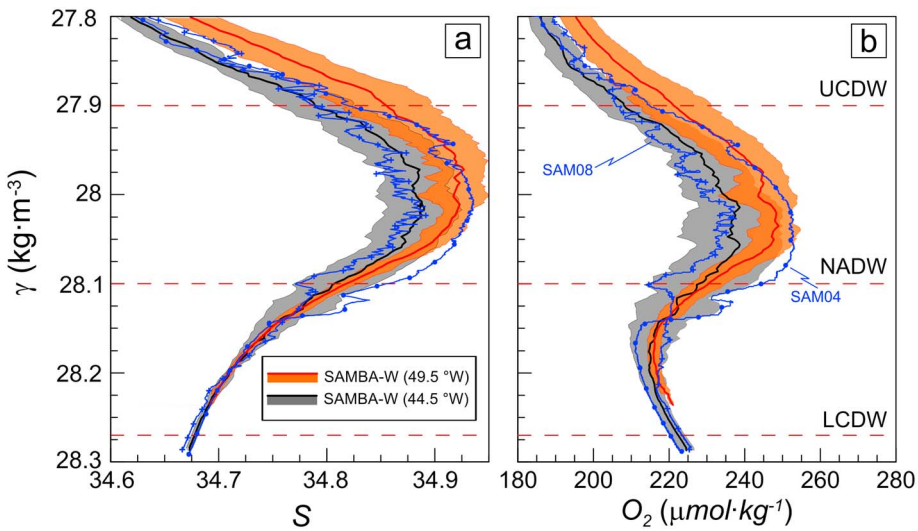

Figure 12. Same as Figure 10 for the deep and abyssal layers except only the profiles at 49.5°W and 44.5°W are shown. Two individual CTD profiles collected at 44.5°W during SAM04 (December 2010) and SAM08 (December 2012) cruises are shown in blue.

Property variations could be introduced by the presence of relatively cold, fresh, and oxygen-rich subantarctic waters advected by migrating eddies detached from the BMC. The other logical possible source for low-salinity surface waters in the region, river outflow from the Río de la Plata, can be excluded as a possibility through analysis of the observed temperature and salinities. Admixtures of TW and Rio de la Plata waters have only been found west of ~51.5°W. This is in agreement with results of Guerrero et al. (2014), who showed that Río de la Plata low-salinity waters do not extend offshore of ~51°W in the vicinity of SAMBA-W. Interannual variability in the BC offshore recirculation may also be associated with the formation of STMW during winter, which is in turn associated with variability of air-sea heat and freshwater fluxes. As discussed in section 4.1, the STMW is advected northward from the formation region to these latitudes by BC offshore recirculation. By contrast, the SACW is characterized by a band of minimum standard deviation, particularly for waters denser than 26.7 kg/m^3. This suggests that the mesoscale activity associated with the BC does not introduce significant water property variability on density surfaces due to the well-mixed nature of the recirculated SACW. At intermediate levels, high variability of AAIW is observed beneath the main southward flow associated to the BC as a consequence of the sporadic presence of lenses of pristine AAIW. Because these younger waters are generally found in the eastern portion of the section, this suggests that the intermediate level is also characterized by mesoscale features such as those previously mentioned. The presence of pristine AAIW at the western end of the SAMBA-W line could also be associated with inversions of the intermediate flow. For example, Preu et al. (2013) found evidence of northward penetrations of young AAIW along the slope as far north as ~31°S on the basis of historical hydrographic data. According to the authors, this may also have an impact on the sediment dynamics in those regions where the AAIW is associated with the near-bottom flow. Although velocity time series derived from the PIES data between 51.5°W and 49.5°W do not show flow reversals beneath the BC, this may be because the PIES velocities represent averages over very large horizontal distances of 90–270 km (Meinen et al., 2012, 2017). The AAIW/UCDW interface is characterized by a band of low variability except over the shelf break, where the interaction with the bottom topography generates local variations. The low variability band suggests a large mixing rate between the two water masses, further supporting the hypothesis that the AAIW and the UCDW share a similar circulation scheme in the western part of the basin.

The intensified variability observed in the deep layers at the eastern end of the SAMBA-W line suggests an energetically meandering DWBC that generates occasional excursions of recently formed NADW away from the continental slope. These property variations are consistent with the strong absolute transport variability observed between 47.5 and 44.5°S, which results in large southward and northward transport anomalies in the offshore portion of the SAMBA-W line (Meinen et al., 2012). Meinen et al. (2017) have associated these

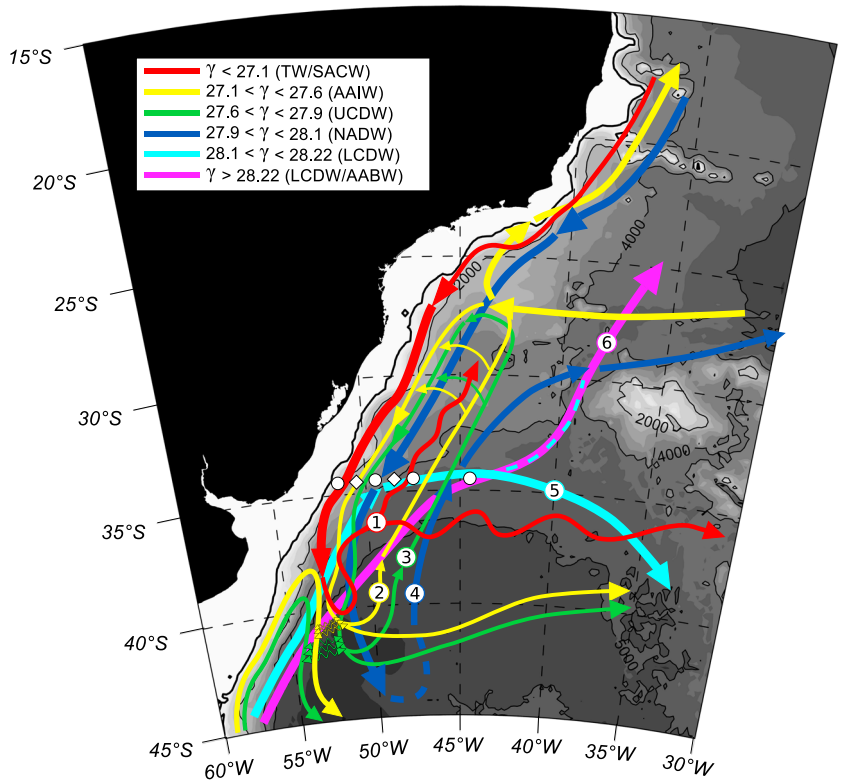

Figure 13. Schematic pathways of the water masses in the northwest Argentine Basin, colored coded according to the different layers defined by neutral density ranges (in kg/m^3) as indicated. The water masses associated to each density range are also indicated. The main pathways are numbered for reference in section 5. The zigzag yellow and green arrows indicate property exchanges in the BMC region, and the dashed paths indicate sporadic or unconfirmed pathways. The white circles (diamonds) indicate the PIES (CPIES) locations along the SAMBA-W line for reference. The bathymetry has been taken from Figure 1.

variations with westward migrating vortices that superimpose on the DWBC and modulate the intensity and sign of the flow in the western portion of the SAMBA-W line. Such vortices could effectively advect the more pristine NADW offshore, as well as inject the recirculated varieties closer to the slope, which is also occasionally observed in some SAMBA-W occupations. Beneath the NADW, the LCDW layer also exhibits high water property variability in the eastern end of the section (Figures 11e and 11f and Table 3). A plausible mechanism for introducing such variability could be the passage of deep eddies detaching from the MC in the Southwest Argentine Basin such as those reported by Gordon and Greengrove (1986a) and Arhan et al. (2002). These eddies could effectively introduce variability by short-circuiting the northward LCDW flow from the Malvinas Escarpment, advecting younger LCDW (i.e., colder and less oxygenated) more effectively to 34.5°S.

5. Summary and Conclusions

High-quality, high-resolution CTD data retrieved from six occupations of the SAMBA-W line, a zonal section extending along 34.5°S between the coast and 44.5°W, were combined with historical CTD and Argo data to analyze the hydrographic conditions and the circulation of the northwestern Argentine Basin. A water mass analysis was conducted focused on modifications, and the results were used to infer likely pathways of the water masses crossing the SAMBA-W line. A snapshot and an average section of the alongshore component of the horizontal velocity measured with LADCP on two of the realizations were also included in the analysis. These measurements collected in 2011–2012 show a vertically coherent southwestward flow throughout the entire water column west of ~49°W and a return flow in the upper 3000 m further offshore. Moreover, the time-averaged section of the meridional component of the velocity (not shown) is in very good

agreement with the average geostrophic velocity as estimated from the PIES as well as numerical models (Meinen et al., 2017) for the period 2009–2014 (their Figures 2a and 2b).

The inferred pathways are summarized in the schematic diagram presented in Figure 13. The upper level circulation is composed of TW and SACW. Both water masses flow southward with the BC close to the continental slope, undergo significant mixing with waters of subantarctic origin at the Brazil-Malvinas front, and recirculate northward across the SAMBA-W line east of ~49.5°W (Figure 13, pathway 1). This pathway is in general agreement with the mean satellite sea surface temperature and sea surface salinity fields (not shown). The properties of the intermediate level waters in the western boundary display a previously undetected recirculation cell superimposed on the well-known pathway beneath the subtropical gyre across the South Atlantic. This pathway resembles that initially proposed by Wust (1935), in which a portion of the recently formed AAIW flows northward along the western boundary. Our results, however, indicate that this northward flow is located about 400–600 km east of the slope. After bifurcating at ~27°S, the "old" AAIW flows southward underneath the BC as an IWBC and crosses the SAMBA-W line close to the shelf break (Figure 13, pathway 2). Mixing with more pristine AAIW varieties, which were advected northward from the Drake Passage by the MC, occurs in the BMC. From the BMC the recirculated AAIW returns equatorward below BC offshore recirculation. Argo data collected between 27°S and 34.5°S show an overall north-to-south salinity decrease in this latitude range, therefore indicating that not only does the recirculation cell extend as far north as the Santos Bifurcation but that the newly formed AAIW leaks into the southward flowing branch below the BC. The water mass analysis yields a similar circulation scheme for the UCDW (Figure 13, pathway 3). The more "pristine" varieties of UCDW are also found in the offshore portion of the SAMBA-W line, whereas the lower portion of this density range is occupied by a warm and light variety of NADW close to the slope.

At the deep levels, the difference between the more recently formed NADW observed close to the continental slope and the more diluted varieties located farther offshore indicates the presence of a DWBC flowing parallel to the continental slope across the SAMBA-W line. Our water mass analysis as well as our LADCP measurements indicate that more pristine NADW flows southward west of ~49.5°W, and diluted varieties recirculate northward through the offshore portion of the section. This is in good agreement with the multiyear time series observations from Meinen et al. (2012) and Meinen et al. (2017). Additionally, given that the eroded, recirculated variety of NADW found at the SAMBA-W line is not observed at 30°S, it must flow eastward into the interior of the basin somewhere between these latitudes (Figure 13, pathway 4). Further investigation is required to determine exactly how the "young" NADW is modified into the eroded form that we observe in the offshore portion of the SAMBA-W line. Previous studies have shown that intense CDW-NADW mixing, causing the strongest circumpolar transformation of CDW, occurs in the southwestern Argentine Basin (Georgi, 1981b). No recirculations are inferred in the abyssal layers from our water mass analysis. However, further analysis using direct velocity measurements must be conducted to fully determine the average sense of the flow. The upper portion of the LCDW (28.10 kg/m^3 $< \gamma <$ 28.22 kg/m^3) flows northward across 34.5°S and is almost absent north of this latitude. As a result, a well-defined deep front separates the NADW to the north from the LCDW to the south, therefore suggesting that the major part of LCDW veers eastward after colliding with the southward flowing NADW in the vicinity of the SAMBA-W line (Figure 13, pathway 5). Denser LCDW and AABW at $\gamma >$ 28.22 kg/m^3 are observed at 27°S and 13°S with overall similarity to that observed at 34.5°S, thus indicating that the waters within this density range cross the SAMBA-W line are not blocked by the NADW (Figure 13, pathway 6). The recirculations documented in this paper may have an important role in the meridional volume transport associated with the South Atlantic MOC, for example, by modifying the density field in the upper levels. The role of the above described recirculations on the large scale net volume, fresh water, and heat transport at the upper, intermediate and deep levels will be further investigated in a subsequent study combining historical CTD and Argo data with numerical model results.

Acknowledgments
The CTD data from the CITHER-2 project are available at http://campagnes.flotteoceanographique.fr/series/15/. The CTD data from the CLIVAR/WOCE A10 occupations as well as the Argo data were obtained from the U.S. NODC World Ocean Database 2013 available at http://www.nodc.noaa.gov/OC5/WOD/pr_wod.html, updated to December 2016. The Argo data were collected and made freely available by the International Argo Program and the national programs that contribute to it (http://www.argo.ucsd.edu and http://argo.jcommops.org). The Argo Program is part of the Global Ocean Observing System. The EKE map was produced from data distributed by E.U. Copernicus Marine Service Information, and the ADT map was downloaded from Aviso http://www.aviso.altimetry.fr). The hydrographic and LACDP data from the SAM cruises are available at ftp://ftp.aoml.noaa.gov/phod/pub/SAM/hydrographic_data/. We thank the captains and crews of R/V Puerto Deseado and R/V Alpha-Crucis who ably supported our work at sea. Marcela Charo processed the CTD data collected in the SAM cruises. This work was financed by the Inter-American Institute for Global Change Research (IAI) grants SGP2076 and CRN3070 (U.S. National Science Foundation grants GEO-0452325 and GEO-1128040) and NOAA Climate Program Office's Ocean Observing and Monitoring Division (FundRef 100007298) under the Southwest Atlantic Meridional Overturning Circulation (SAM) project, with additional support from the NOAA Atlantic Oceanographic and Meteorological Laboratory. The Brazilian component of the research was funded by the São Paulo State Funding Agency (FAPESP) (grant 2011/50552-4). D. Valla was supported by a fellowship from Consejo Nacional de Investigaciones Científicas y Técnicas, Argentina, and the Argentine Presidential Fellowship in Science and Technology Program sponsored by the Argentine government and the Argentine Fulbright Commission. The participation of C. S. Meinen was supported via the NOAA Climate Program Office's Ocean Observing and Monitoring Division (FundRef 100007298) under the Southwest Atlantic Meridional Overturning Circulation (SAM) project, with additional support from the NOAA Atlantic Oceanographic and Meteorological Laboratory. E. Campos acknowledges a CNPq Fellowship (grant 302018/2014-0). We thank the anonymous reviewers whose comments on earlier drafts of this manuscript helped improving the final presentation of the results.

References

Ansorge, I. J., Baringer, M. O., Campos, E. J. D., Dong, S., Fine, R. A., Garzoli, S. L., et al. (2014). Basin-Wide Oceanographic Array Bridges the South Atlantic. *Eos, Transactions American Geophysical Union*, *95*(6), 53–54. https://doi.org/10.1002/2014EO060001

Arhan, M., Carton, X., Piola, A., & Zenk, W. (2002). Deep lenses of circumpolar water in the Argentine Basin. *Journal of Geophysical Research*, *107*(C1), 3007. https://doi.org/10.1029/2001JC000963

Arhan, M., Heywood, K. J., & King, B. A. (1999). The deep waters from the Southern Ocean at the entry to the Argentine Basin. *Deep-Sea Research Part II: Topical Studies in Oceanography*, *46*(1–2), 475–499. https://doi.org/10.1016/S0967-0645(98)00110-6

Boebel, O., Davis, R. E., Ollitrault, M., Peterson, R. G., Richardson, P. L., Schmid, C., & Zenk, W. (1999). The intermediate depth circulation of the western South Atlantic. *Geophysical Research Letters*, *26*(21), 3329–3332. https://doi.org/10.1029/1999GL002355

Bower, A. S., & Hunt, H. D. (2000). Lagrangian observations of the Deep Western Boundary Current in the North Atlantic Ocean. Part I: Large-scale pathways and spreading rates. *Journal of Physical Oceanography*, *30*(5), 764–783. https://doi.org/10.1175/1520-0485(2000)030<0764:LOOTDW>2.0.CO;2

Bower, A. S., Lozier, M. S., Gary, S. F., & Boning, C. W. (2009). Interior pathways of the North Atlantic Meridional Overturning Circulation. *Nature*, *459*(7244), 243–247. https://doi.org/10.1038/nature07979

Boyer, T. P., Antonov, J. I., Baranova, O. K., Coleman, C., Garcia, H. E., Grodsky, A., et al. (2013). In S. Levitus & A. Mishonov (Eds.), *World Ocean Database 2013*, *NOAA Atlas NESDIS* (Vol. 72, p. 209). Silver Spring, MD: National Oceanic and Atmospheric Administration.

Brandini, F. P., Boltovskoy, D., Piola, A., Kocmur, S., Röttgers, R., Cesar Abreu, P., & Mendes Lopes, R. (2000). Multiannual trends in fronts and distribution of nutrients and chlorophyll in the southwestern Atlantic (30–62°S). *Deep-Sea Research Part I: Oceanographic Research Papers*, *47*(6), 1015–1033. https://doi.org/10.1016/S0967-0637(99)00075-8

Coles, V. J., McCartney, M. S., Olson, D. B., & Smethie, W. M. (1996). Changes in Antarctic Bottom Water properties in the western South Atlantic in the late 1980s. *Journal of Geophysical Research*, *101*(C4), 8957–8970. https://doi.org/10.1029/95JC03721

Dengler, M., Schott, F. A., Eden, C., Brandt, P., Fischer, J., & Zantopp, R. J. (2004). Break-up of the Atlantic deep western boundary current into eddies at 8°S. *Nature*, *432*(7020), 1018–1020. https://doi.org/10.1038/nature03134

Dong, S., Baringer, M. O., Goni, G. J., Meinen, C. S., & Garzoli, S. L. (2014). Seasonal variations in the South Atlantic Meridional Overturning Circulation from observations and numerical models. *Geophysical Research Letters*, *41*, 4611–4618. https://doi.org/10.1002/2014GL060428

Dong, S., Garzoli, S., Baringer, M., Meinen, C., & Goni, G. (2009). Interannual variations in the Atlantic Meridional Overturning Circulation and its relationship with the net northward heat transport in the South Atlantic. *Geophysical Research Letters*, *36*, L20606. https://doi.org/10.1029/2009GL039356

Frajka-Williams, E., Meinen, C. S., Johns, W. E., Smeed, D. A., Duchez, A., Lawrence, A. J., et al. (2016). Compensation between meridional flow components of the Atlantic MOC at 26°N. *Ocean Science*, *12*(2), 481–493. https://doi.org/10.5194/os-12-481-2016

Ganopolski, A., & Rahmstorf, S. (2001). Rapid changes of glacial climate simulated in a coupled climate model. *Nature*, *409*(6817), 153–158. https://doi.org/10.1038/35051500

Garzoli, S. L. (1993). Geostrophic velocity and transport variability in the Brazil-Malvinas Confluence. *Deep Sea Research Part I: Oceanographic Research Papers*, *40*(7), 1379–1403. https://doi.org/10.1016/0967-0637(93)90118-M

Garzoli, S. L., Dong, S., Fine, R., Meinen, C. S., Perez, R. C., Schmid, C., et al. (2015). The fate of the Deep Western Boundary Current in the South Atlantic. *Deep Sea Research Part I: Oceanographic Research Papers*, *103*, 125–136. https://doi.org/10.1016/j.dsr.2015.05.008

Garzoli, S. L., & Matano, R. (2011). The South Atlantic and the Atlantic Meridional Overturning Circulation. *Deep Sea Research Part II: Topical Studies in Oceanography*, *58*(17–18), 1837–1847. https://doi.org/10.1016/j.dsr2.2010.10.063

Georgi, D. T. (1981a). Circulation of bottom waters in the southwestern South Atlantic. *Deep Sea Research Part A. Oceanographic Research Papers*, *28*(9), 959–979. https://doi.org/10.1016/0198-0149(81)90012-1

Georgi, D. T. (1981b). On the relationship between the large-scale property variations and fine structure in the Circumpolar Deep Water. *Journal of Geophysical Research*, *86*(C7), 6556–6566. https://doi.org/10.1029/JC086iC07p06556

Gordon, A. L. (1981). South Atlantic thermocline ventilation. *Deep Sea Research Part A, Oceanographic Research Papers*, *28*(11), 1239–1264. https://doi.org/10.1016/0198-0149(81)90033-9

Gordon, A. L., & Greengrove, C. L. (1986a). Abyssal eddy in the southwest Atlantic. *Deep Sea Research Part A. Oceanographic Research Papers*, *33*(6), 839–847. https://doi.org/10.1016/0198-0149(86)90091-9

Gordon, A. L., & Greengrove, C. L. (1986b). Geostrophic circulation of the Brazil-Falkland confluence. *Deep Sea Research Part A. Oceanographic Research Papers*, *33*(5), 573–585. https://doi.org/10.1016/0198-0149(86)90054-3

Gordon, A. L., Weiss, R. F., Smethie, W. M., & Warner, M. J. (1992). Thermocline and intermediate water communication between the South Atlantic and Indian oceans. *Journal of Geophysical Research*, *97*(C5), 7223–7240. https://doi.org/10.1029/92JC00485

Guerrero, R. A., Piola, A. R., Fenco, H., Matano, R. P., Combes, V., Chao, Y., et al. (2014). The salinity signature of the cross-shelf exchanges in the southwestern Atlantic Ocean: Satellite observations. *Journal of Geophysical Research: Oceans*, *119*, 7794–7810. https://doi.org/10.1002/2014JC010113

Hummels, R., Brandt, P., Dengler, M., Fischer, J., Araujo, M., Veleda, D., & Durgadoo, J. V. (2015). Interannual to decadal changes in the western boundary circulation in the Atlantic at 11°S. *Geophysical Research Letters*, *42*, 7615–7622. https://doi.org/10.1002/2015GL065254

IOC, IHO, and BODC (2003). Centenary Edition of the GEBCO Digital Atlas, Edited, Intergovernmental Oceanographic Commission and the International Hydrographic Organization as part of the General Bathymetric Chart of the Oceans, British Oceanographic Data Centre.

Jackett, D. R., & McDougall, T. J. (1997). A neutral density variable for the world's oceans. *Journal of Physical Oceanography*, *27*(2), 237–263. https://doi.org/10.1175/1520-0485(1997)027<0237:ANDVFT>2.0.CO;2

Langdon, C. (2010). Determination of dissolved oxygen in seawater by Winkler titration using the amperometric technique, IOCCP rep. 14, ICPO Publ. Ser. 134, Version 1 (pp. 1–18).

Legeais, J.-F., Ollitrault, M., & Arhan, M. (2013). Lagrangian observations in the Intermediate Western Boundary Current of the South Atlantic. *Deep Sea Research Part II: Topical Studies in Oceanography*, *85*, 109–126. https://doi.org/10.1016/j.dsr2.2012.07.028

Lozier, M. S., Gary, S. F., & Bower, A. S. (2013). Simulated pathways of the overflow waters in the North Atlantic: Subpolar to subtropical export. *Deep Sea Research Part II: Topical Studies in Oceanography*, *85*(Supplement C), 147–153. https://doi.org/10.1016/j.dsr2.2012.07.037

Lumpkin, R., & Garzoli, S. (2011). Interannual to decadal changes in the western South Atlantic's surface circulation. *Journal of Geophysical Research*, *116*, C01014. https://doi.org/10.1029/2010JC006285

Lumpkin, R., & Speer, K. (2007). Global Ocean Meridional Overturning. *Journal of Physical Oceanography*, *37*(10), 2550–2562. https://doi.org/10.1175/JPO3130.1

Lutjeharms, J. R. E. (1996). The exchange of water between the South Indian and South Atlantic Oceans. In G. Wefer, W. H. Berger, G. Siedler, & D. J. Webb (Eds.), *The South Atlantic: Present and Past Circulation* (pp. 125–162). Berlin, Heidelberg: Springer. https://doi.org/10.1007/978-3-642-80353-6_8

McCarthy, G. D., Smeed, D. A., Johns, W. E., Frajka-Williams, E., Moat, B. I., Rayner, D., et al. (2015). Measuring the Atlantic Meridional Overturning Circulation at 26°N. *Progress in Oceanography*, *130*, 91–111. https://doi.org/10.1016/j.pocean.2014.10.006

Meinen, C. S., Garzoli, S. L., Perez, R. C., Campos, E., Piola, A. R., Chidichimo, M. P., et al. (2017). Characteristics and causes of Deep Western Boundary Current transport variability at 34.5°S during 2009–2014. *Ocean Science*, *13*(1), 175–194. https://doi.org/10.5194/os-13-175-2017

Meinen, C. S., Piola, A. R., Perez, R. C., & Garzoli, S. L. (2012). Deep Western Boundary Current transport variability in the South Atlantic: Preliminary results from a pilot array at 34.5° S. *Ocean Science*, *8*(6), 1041–1054. https://doi.org/10.5194/os-8-1041-2012

Meinen, C. S., Speich, S., Perez, R. C., Dong, S., Piola, A. R., Garzoli, S. L., et al. (2013). Temporal variability of the meridional overturning circulation at 34.5°S: Results from two pilot boundary arrays in the South Atlantic. *Journal of Geophysical Research: Oceans*, *118*, 6461–6478. https://doi.org/10.1002/2013JC009228

Mémery, L., Arhan, M., Alvarez-Salgado, X. A., Messias, M. J., Mercier, H., Castro, C. G., & Rios, A. F. (2000). The water masses along the western boundary of the south and equatorial Atlantic. *Progress in Oceanography*, *47*(1), 69–98. https://doi.org/10.1016/s0079-6611 (00)00032-x

Mémery, L., Arhan, M., Billant, A., Branellec, P., & Mercier, H. (1995). Campagne CITHER 2 N/O Maurice Ewing 4 janvier-21 mars 1994. Recueil de Données. Volume 2: Données CTD-O2. Rep.

Müller, T. J., Ikeda, Y., Zangenberg, N., & Nonato, L. V. (1998). Direct measurements of western boundary currents off Brazil between 20°S and 28°S. *Journal of Geophysical Research*, *103*(C3), 5429–5437. https://doi.org/10.1029/97JC03529

Orsi, A. H., Johnson, G. C., & Bullister, J. L. (1999). Circulation, mixing, and production of Antarctic Bottom Water. *Progress in Oceanography*, *43*(1), 55–109. https://doi.org/10.1016/S0079-6611 (99)00004-X

Perez, R. C., Baringer, M. O., Dong, S., Garzoli, S. L., Goes, M., Goni, G. J., et al. (2015). Measuring the Atlantic Meridional Overturning Circulation. *Marine Technology Society Journal*, *49*(2), 167–177. https://doi.org/10.4031/MTSJ.49.2.14

Peterson, L. C., Haug, G. H., Hughen, K. A., & Röhl, U. (2000). Rapid changes in the hydrologic cycle of the tropical Atlantic during the last glacial. *Science*, *290*(5498), 1947–1951. https://doi.org/10.1126/science.290.5498.1947

Piola, A. R., Campos, E. J. D., Möller, O. O. Jr., Charo, M., & Martinez, C. (2000). Subtropical shelf front off eastern South America. *Journal of Geophysical Research*, *105*(C3), 6565–6578. https://doi.org/10.1029/1999JC000300

Piola, A. R., & Georgi, D. T. (1982). Circumpolar properties of Antarctic intermediate water and Subantarctic Mode Water. *Deep Sea Research Part A, Oceanographic Research Papers*, *29*(6), 687–711. https://doi.org/10.1016/0198-0149(82)90002-4

Piola, A. R., & Gordon, A. L. (1989). Intermediate waters in the southwest South Atlantic. *Deep Sea Research Part A, Oceanographic Research Papers*, *36*(1), 1–16. https://doi.org/10.1016/0198-0149(89)90015-0

Preu, B., Hernández-Molina, F. J., Violante, R., Piola, A. R., Paterlini, C. M., Schwenk, T., et al. (2013). Morphosedimentary and hydrographic features of the northern Argentine margin: The interplay between erosive, depositional and gravitational processes and its conceptual implications. *Deep Sea Research Part I: Oceanographic Research Papers*, *75*, 157–174. https://doi.org/10.1016/j.dsr.2012.12.013

Provost, C., Escoffier, C., Maamaatuaiahutapu, K., Kartavtseff, A., & Garçon, V. (1999). Subtropical mode waters in the South Atlantic Ocean. *Journal of Geophysical Research*, *104*(C9), 21,033–21,049. https://doi.org/10.1029/1999JC900049

Reid, J. L. (1989). On the total geostrophic circulation of the South Atlantic Ocean: Flow patterns, tracers, and transports. *Progress in Oceanography*, *23*(3), 149–244. https://doi.org/10.1016/0079-6611(89)90001-3

Reid, J. L., Nowlin, W. D. Jr., & Patzert, W. C. (1977). On the characteristics and circulation of the southwestern Atlantic Ocean. *Journal of Physical Oceanography*, *7*(1), 62–91. https://doi.org/10.1175/1520-0485(1977)007<0062:OTCACO>2.0.CO;2

Rhein, M., Kieke, D., & Steinfeldt, R. (2015). Advection of North Atlantic Deep Water from the Labrador Sea to the southern hemisphere. *Journal of Geophysical Research: Oceans*, *120*, 2471–2487. https://doi.org/10.1002/2014JC010605

Rhein, M., Stramma, L., & Send, U. (1995). The Atlantic Deep Western Boundary Current: Water masses and transports near the equator. *Journal of Geophysical Research*, *100*(C2), 2441–2457. https://doi.org/10.1029/94JC02355

Rintoul, S. R. (1991). South Atlantic interbasin exchange. *Journal of Geophysical Research*, *96*(C2), 2675–2692. https://doi.org/10.1029/90JC02422

Sato, O. T., & Polito, P. S. (2014). Observation of South Atlantic subtropical mode waters with Argo profiling float data. *Journal of Geophysical Research: Oceans*, *119*, 2860–2881. https://doi.org/10.1002/2013JC009438

Schmid, C. (2000). Dynamics of Intermediate Water Circulation in the Subtropical South Atlantic. *Journal of Physical Oceanography*, *30*(12), 3191–3211. https://doi.org/10.1175/1520-0485(2000)030<3191:DOIWCI>2.0.CO;2

van Sebille, E., Johns, W. E., & Beal, L. M. (2012). Does the vorticity flux from Agulhas rings control the zonal pathway of NADW across the South Atlantic? *Journal of Geophysical Research*, *117*, C05037. https://doi.org/10.1029/2011JC007684

Send, U., Lankhorst, M., & Kanzow, T. (2011). Observation of decadal change in the Atlantic Meridional Overturning Circulation using 10 years of continuous transport data. *Geophysical Research Letters*, *38*, L24606. https://doi.org/10.1029/2011GL049801

Speer, K. G., & Zenk, W. (1993). The flow of Antarctic Bottom Water into the Brazil Basin. *Journal of Physical Oceanography*, *23*(12), 2667–2682. https://doi.org/10.1175/1520-0485(1993)023<2667:TFOABW>2.0.CO;2

Speich, S., Blanke, B., & Cai, W. (2007). Atlantic Meridional Overturning Circulation and the Southern Hemisphere supergyre. *Geophysical Research Letters*, *34*, L23614. https://doi.org/10.1029/2007GL031583

Srokosz, M. A., & Bryden, H. L. (2015). Observing the Atlantic Meridional Overturning Circulation yields a decade of inevitable surprises. *Science*, *348*(6241), 1255575. https://doi.org/10.1126/science.1255575

Stott, L., Poulsen, C., Lund, S., & Thunell, R. (2002). Super ENSO and global climate oscillations at millennial time scales. *Science*, *297*(5579), 222–226. https://doi.org/10.1126/science.1071627

Stramma, L., & Peterson, R. G. (1990). The South Atlantic Current. *Journal of Physical Oceanography*, *20*(6), 846–859. https://doi.org/10.1175/1520-0485(1990)020<0846:TSAC>2.0.CO;2

Talley, L. D. (1996). Antarctic Intermediate Water in the South Atlantic. In G. Wefer, W. H. Berger, G. Siedler, & D. J. Webb (Eds.), *The South Atlantic: Present and Past Circulation* (pp. 219–238). Berlin, Heidelberg: Springer. https://doi.org/10.1007/978-3-642-80353-6_11

Thurnherr, A. M. (2010). A practical assessment of the errors associated with full-depth LADCP profiles obtained using Teledyne RDI workhorse acoustic Doppler current profilers. *Journal of Atmospheric and Oceanic Technology*, *27*(7), 1215–1227. https://doi.org/10.1175/2010JTECHO708.1

Trenberth, K. E., & Caron, J. M. (2001). Estimates of meridional atmosphere and ocean heat transports. *Journal of Climate*, *14*(16), 3433–3443. https://doi.org/10.1175/1520-0442(2001)014<3433:EOMAAO>2.0.CO;2

Tsuchiya, M., Talley, L. D., & McCartney, M. S. (1994). Water-mass distributions in the western South Atlantic: A section from South Georgia Island (54S) northward across the equator. *Journal of Marine Research*, *52*(1), 55–81. https://doi.org/10.1357/0022240943076759

Uchida, H., Fukasawa, M., & Murata, A. (2005). WHP P6, A10, I3/I4 REVISIT DATA BOOK Blue Earth Global Expedition 2003 (BEAGLE2003) Volume 1, 2. JAMSTEC Publication.

Vellinga, M., & Wood, R. A. (2002). Global climatic impacts of a collapse of the Atlantic thermohaline circulation. *Climatic Change*, *54*(3), 251–267. https://doi.org/10.1023/A:1016168827653

Visbeck, M. (2002). Deep velocity profiling using lowered acoustic Doppler current profilers: Bottom track and inverse solutions. *Journal of Atmospheric and Oceanic Technology*, *19*(5), 794–807. https://doi.org/10.1175/1520-0426(2002)019<0794:DVPULA>2.0.CO;2

Wanninkhof, R., Feely, R., Millero, F., Carlson, C., O'Neil Baringer, M., Macdonald, A., et al. (2013). Carbon dioxide, hydrographic, and chemical data obtained during the R/V Ronald H. Brown in the Atlantic Ocean on CLIVAR repeat hydrography section A10 (September 26 - October 31, 2011). http://cdiac.ornl.gov/ftp/oceans/CLIVAR/A10_2011/. Carbon Dioxide Information Analysis Center, Oak Ridge National Laboratory, US Department of Energy, Oak Ridge, Tennessee. https://doi.org/10.3334/CDIAC/OTG.CLIVAR_A10_2011

Watts, D. R. (1991). Equatorward currents in temperatures 1.8–6.0°C on the continental slope in the mid-Atlantic Bight. In P. C. Chu & J. C. Gascard (Eds.), *Elsevier Oceanography Series* (pp. 183–196). Elsevier. https://doi.org/10.1016/S0422-9894 (08)70067-9

Wust, G. (1935). Schichtung und Zirkulation des Atlantischen Ozeans. Die Stratophäre. In *Wissenschaftliche Ergebnisse der Deutschen Atlantischen Expedition auf dem Forschungs—und Vermessungsschiff "Meteor" 1925–1927* (Vol. 6, first part, 2, 180 pp.). (The Stratosphere of the Atlantic Ocean, Emery, W.J. (Ed), 1978 Amerind, New Delhi, 112 pp.). Verlag von Walter de Gruyter & CO.

Zangenberg, N., & Siedler, G. (1998). Path of the North Atlantic Deep Water in the Brazil Basin. *Journal of Geophysical Research*, *103*(C3), 5419–5428. https://doi.org/10.1029/97JC03287

Zhang, L., & Wang, C. (2013). Multidecadal North Atlantic sea surface temperature and Atlantic Meridional Overturning Circulation variability in CMIP5 historical simulations. *Journal of Geophysical Research*, *118*, 5772–5791. https://doi.org/10.1002/jgrc.20390

Zhang, L., Wang, C., & Lee, S.-K. (2014). Potential role of Atlantic Warm Pool-induced freshwater forcing in the Atlantic Meridional Overturning Circulation: Ocean–sea ice model simulations. *Climate Dynamics*, *43*(1-2), 553–574. https://doi.org/10.1007/s00382-013-2034-z